Actin assembly and non-muscle myosin activity drive dendrite retraction in an UNC-6/Netrin dependent self-avoidance response.

Lakshmi Sundararajan,[1] Cody J. Smith,[1,2] Joseph D. Watson[3,4], Bryan A. Millis[1,5,6], Matthew J. Tyska, [1] David M. Miller, III[1,4,7]

[1]Department of Cell and Developmental Biology, Vanderbilt University, Nashville, TN

[2]Current address: Department of Biological Sciences, Notre Dame University, South Bend, IN

[3]Current address: Rho, Chapel Hill, NC

[4]Neuroscience Graduate Program, Vanderbilt University, Nashville, TN

[5]Cell Imaging Shared Resource, Vanderbilt University, Nashville, TN

[6]Vanderbilt Biophotonics Center, Vanderbilt University, Nashville, TN

[7]Corresponding author

ABSTRACT

Dendrite growth is constrained by a self-avoidance response that induces retraction but the downstream pathways that balance these opposing mechanisms are unknown. We have proposed that the diffusible cue UNC-6(Netrin) is captured by UNC-40(DCC) for a short-range interaction with UNC-5 to trigger self-avoidance in the *C. elegans* PVD neuron. Here we report that the actin-polymerizing proteins UNC-34(Ena/VASP), WSP-1(WASP), UNC-73(Trio), MIG-10(Lamellipodin) and the Arp2/3 complex effect dendrite retraction in the self-avoidance response mediated by UNC-6(Netrin). The paradoxical idea that actin polymerization results in shorter rather than longer dendrites is explained by our finding that NMY-1 (non-muscle myosin II) is necessary for retraction and could therefore mediate this effect in a contractile mechanism. Our results also show that dendrite length is determined by the antagonistic effects on the actin cytoskeleton of separate sets of effectors for retraction mediated by UNC-6(Netrin) versus outgrowth promoted by the DMA-1 receptor. Thus, our findings suggest that the dendrite length depends on an intrinsic mechanism that balances distinct modes of actin assembly for growth versus retraction.

AUTHOR SUMMARY

Neurons may extend highly branched dendrites to detect input over a broad receptive field. The formation of actin filaments may drive dendrite elongation. The architecture of the dendritic arbor also depends on mechanisms that limit expansion. For example, sister dendrites from a single neuron usually do not overlap due to self-avoidance. Although cell surface proteins are known to mediate self-avoidance, the downstream pathways that drive dendrite retraction in this phenomenon are largely unknown. Studies of the highly branched PVD sensory neuron in *C. elegans* have suggested a model of self-avoidance in which the UNC-40/DCC receptor captures the diffusible cue UNC-6/Netrin at the tips of PVD dendrites where it interacts with the UNC-5 receptor on an opposing sister dendrite to induce retraction. Here we report genetic evidence that UNC-5-dependent retraction requires downstream actin polymerization. This finding evokes a paradox: How might actin polymerization drive both dendrite growth and retraction? We propose two answers: (1) Distinct sets of effectors are involved in actin assembly for growth vs retraction; (2) Non-muscle myosin interacts with a nascent actin assemblage to trigger retraction. Our results show that dendrite length depends on the balanced effects of specific molecular components that induce growth vs retraction.

62 **INTRODUCTION**

63 Dendritic arbors are defined by the balanced effects of outgrowth which expands the structure
64 versus retraction which constrains the size of the receptive field. Microtubules and filamentous
65 actin (F-actin) are prominent dendritic components and have been implicated as key drivers of
66 dendritic growth and maintenance by the finding that treatments that perturb cytoskeletal dynamics
67 may also disrupt dendritic structure [1-3]. For many neurons, dendritic growth is highly exuberant
68 with multiple tiers of branches projecting outward from the cell soma. Ultimately, growth may be
69 terminated by external cues. For example, neurons with similar functions are typically limited to
70 separate domains by tiling mechanisms in which mutual contact induces dendrite retraction. The
71 related phenomenon of self-avoidance is widely employed to prevent overlaps among sister
72 dendrites arising from a single neuron [4]. Homotypic interactions between the membrane
73 components Dscam and protocaderins can mediate the self-avoidance response [5-7]. Surprisingly,
74 in some instances, soluble axon guidance cues and their canonical receptors are also required. For
75 example, self-avoidance for the highly-branched Purkinje neuron depends on both protocadherins
76 and also repulsive interactions between sister dendrites decorated with the Robo receptor and its
77 diffusible ligand, Slit [8]. In another example, we have shown that UNC-6/Netrin and its cognate
78 receptors, UNC-5 and UNC-40/DCC, mediate self-avoidance for PVD nociceptive neurons in *C.*
79 *elegans* [9]. Although multiple cell-surface interactions are now known to trigger self-avoidance,
80 little is known of the downstream effectors that drive dendrite retraction in this mechanism.

81

82 The PVD neurons, one on each side of the body, build complex dendritic arbors through a series
83 of successive 1°, 2°, 3° and 4° orthogonal branching events [10] [11-13]. Self-avoidance ensures
84 that adjacent 3° branches do not overgrow one another [9,11] (Figure S1). Our previous results

85 suggested a novel mechanism of self-avoidance in which UNC-40/DCC captures UNC-6/Netrin
86 at the PVD cell surface and then triggers retraction by interacting with UNC-5 on the neighboring
87 3° branch. UNC-40/DCC may also effect self-avoidance by acting in a separate pathway that does
88 not involve UNC-6/Netrin [9]. Here we describe a cell biological model of dendrite retraction in
89 the PVD self-avoidance response that depends on actin polymerization.

90 The structure of the actin cytoskeleton is controlled by a wide array of effector proteins that
91 regulate specific modes of actin polymerization. For example, Ena/VASP enhances F-actin
92 elongation at the plus-end [12] and the Arp2/3 complex functions with WASP (Wiskott-Aldrich
93 syndrome protein) and the Wave Regulatory Complex (WRC) to promote F-actin branching [13].
94 Upstream regulators of WASP and the WRC include Rho family GTPases [14] and their activators,
95 the GEFs (Guanine nucleotide Exchange Factors) UNC-73/Trio [15,16] and TIAM (T-cell
96 Lymphoma Invasion and Metastasis Factor) [17,18]. Members of the Lamellipodin/Lpd family
97 recruit Ena/VASP to localize F-actin assembly at the leading edge of migrating cells [19]. The fact
98 that all of these components (UNC-34/Ena/VASP, Arp2/3 complex, WSP-1/WASP, WRC, UNC-
99 73/Trio, TIAM/TIAM-1, MIG-10/lamellipodin) have been previously shown to function in *C.*
100 *elegans* to mediate axon guidance underscores the key role of the actin cytoskeleton in growth
101 cone steering [15,18,20-23].

102

103 Our results show that UNC-34/Ena/VASP functions downstream of UNC-5 to mediate PVD self-
104 avoidance. Genetic evidence detecting roles for the Arp2/3 complex and its upstream regulator,
105 WASP/WSP-1, indicates that the formation of branched actin networks may contribute to dendrite
106 retraction. A necessary role for actin polymerization is also indicated by the defective PVD self-

107 avoidance response of mutants with disabled UNC-73/Trio or MIG-10/lamellipodin. We show that
108 PVD self-avoidance also requires NMY-1/non-muscle myosin II which we propose effects
109 dendrite retraction in a contractile mechanism that drives the reorganization of the nascent actin
110 cytoskeleton. The necessary role for myosin could explain how actin polymerization can result in
111 shorter rather than longer dendrites in the self-avoidance response. Thus, we propose that UNC-
112 6/Netrin triggers self-avoidance by simultaneously stimulating actin assembly and non-muscle
113 myosin activity in 3° dendrites.
114
115 Because dendrite growth depends on actin polymerization [24,25], our finding that the actin
116 cytoskeleton is also necessary for dendrite self-avoidance points to different modes of actin
117 polymerization for growth *vs* retraction. Recent work has shown that a multicomponent complex
118 involving the PVD membrane proteins DMA-1 and HPO-30 drives dendritic growth by linking
119 the PVD actin cytoskeleton to adhesive cues on the adjacent epidermis [26,27]. Dendrite
120 elongation, in this case, depends on the WRC and TIAM-1, both of which are known to promote
121 actin polymerization. In contrast, our work has revealed that effectors of actin polymerization that
122 are required for 3° branch self-avoidance (e.g., UNC-34/Ena/VASP, MIG-10/lamellipodin, UNC-
123 73/Trio, Arp2/3 complex, WSP-1/WASP) are not necessary for 3° dendrite outgrowth.
124 Additionally, we show that UNC-6/Netrin signaling antagonizes the DMA-1-dependent
125 mechanism of dendritic growth. These findings are significant because they suggest that overall
126 dendrite length is defined by the relative strengths of opposing pathways that utilize separate sets
127 of effectors to differentially regulate actin polymerization for either growth or retraction.
128

129 **RESULTS**

130 **UNC-6/Netrin mediates PVD sister dendrite self-avoidance.**

131 To visualize PVD morphology, we utilized a previously characterized GFP marker driven by a
132 PVD-specific promoter (*PVD*::GFP) (Figure S1A-B) [11]. Each PVD neuron adopts a
133 stereotypical morphology characterized by a series of orthogonal junctions between adjacent
134 branches: 1° dendrites extend laterally from the PVD cell soma; each 2° dendrite projects along
135 the dorsal-ventral axis to generate a T-shaped junction comprised of two 3° dendrites each with
136 either an anterior or posterior trajectory; terminal 4° dendrites occupy interstitial locations between
137 the epidermis and body muscles. The net result of this branching pattern is a series of tree-like
138 structures or menorahs distributed along the 1° dendrite. In contrast to the highly branched
139 dendritic architecture, a single axon projects from the PVD cell soma to join the ventral nerve cord
140 [10,11,26]. Despite the complexity of this network, dendrites rarely overlap (< 5%) in the mature
141 PVD neuron (Figure S1A) [9]. Self-avoidance depends on an active process in which sister PVD
142 dendrites retract upon physical contact with one another (Figure S1C). In the wild type, 3° branches
143 arising from adjacent menorahs initially grow outward toward one another but then retract after
144 mutual contact. The net result is a characteristic gap between the tips of 3° dendrites in neighboring
145 menorahs [11]. We have previously shown that 3° dendrite self-avoidance depends in part on the
146 diffusible cue UNC-6/Netrin and its canonical receptors, UNC-40/DCC and UNC-5 [9]. Mutations
147 that disable *unc-6*, for example, result in a significant increase in the fraction of 3° dendrites that
148 fail to retract and remain in contact (Figure S1B, Figure 3D). Similar self-avoidance defects were
149 observed for mutants of either *unc-40* or *unc-5*. Our results are consistent with a model in which
150 UNC-40 captures UNC-6 for contact with UNC-5 at the tips of adjacent 3° dendrites (Figure

151 S1D)[9]. Here we address the question of how the activated UNC-5 receptor then modifies the
152 actin cytoskeleton to drive dendrite retraction.
153
154 **Constitutively active UNC-5 delays dendrite outgrowth:**
155 We have proposed that UNC-6 initiates dendrite retraction by activating UNC-5 [9]. This model
156 predicts that a constitutively active form of UNC-5 should retard net outgrowth of 3º dendrites by
157 triggering an opposing retraction mechanism. To test this idea, we attached a myristoylation
158 sequence to the cytoplasmic domain of UNC-5 [27]. The resultant myristyolated UNC-5
159 intracellular domain (MYR::UNC-5) is effectively tethered to the cytoplasmic membrane which
160 is sufficient to activate UNC-5 dependent downstream signaling [27]. Expression of MYR::UNC-
161 5 in PVD results in substantially shorter 3° dendrites in comparison to wild type at the L3 stage
162 (Figure 1A-C). This phenotype suggests that constitutive activation of UNC-5 impairs normal
163 outgrowth of 3° dendrites. We tested this idea by scoring the dynamic status of 3° dendrites. To
164 quantify movement, we measured the distance from a fiduciary point to the tip of a 3° dendrite at
165 intervals over time (delta t = 240 sec) (Figure 1E) (Movies S1-S2). Examples of these
166 measurements are shown in Figure 1E. We observed that wild-type 3° dendrites typically display
167 saltatory movement with periodic bouts of extension and retraction that result in net elongation. In
168 contrast, 3° dendrites of PVD neurons expressing MYR::UNC-5 grow more slowly and rarely
169 show periods of active extension and retraction (Figures 1E and 1F). The higher overall motility
170 of 3° dendrites in the wild-type vs PVD::MYR::UNC-5 strain is evident from a comparison of the
171 standard deviation of the net movement of 3° dendrites from a fiduciary point in each strain (Figure
172 1F). Despite slower outgrowth, 3° dendrites expressing MYR::UNC-5 eventually produce a
173 normal-appearing PVD architecture by the late L4 stage (Figure 2A). MYR::UNC-5 lacks the

174 extracellular UNC-6-binding domain (Figure 1D) and thus should function independently of UNC-
175 6. We confirmed this prediction by demonstrating that MYR::UNC-5 prevents the self-avoidance
176 defect observed in an *unc-6* mutant in L4 stage animals (Figure 2B, D). We attribute this effect to
177 the constitutive activation of dendrite retraction by MYR::UNC-5 that effectively prevents
178 overgrowth of adjacent sister 3° dendrites in an *unc-6/Netrin* mutant. Together, these results are
179 consistent with the hypothesis that UNC-5 functions downstream of UNC-6/Netrin to trigger
180 dendrite retraction in the self-avoidance response.
181
182 **UNC-34/Ena/VASP mediates self-avoidance in actin-containing PVD dendrites.**
183 To explore potential modifications of the PVD cytoskeleton as effectors of the UNC-6/Netrin-
184 dependent self-avoidance response, we used live cell markers to visualize actin (PVD::ACT-
185 1::GFP) and microtubules (*pdes-2*::TBA-1::mCherry) in PVD [28]. We observed a robust ACT-
186 1::GFP signal throughout the PVD neuron including the axon and all dendrites (Figure 3A). In
187 contrast, the TBA-1::mCherry signal was strongest in the PVD axon and 1° dendrite. This result
188 confirms an earlier report suggesting that dendritic microtubules are most abundant in the 1°
189 branch (Figure 3A) [28]. We thus considered the possibility that the self-avoidance response could
190 depend on the regulation of actin dynamics. To test this idea, we examined the PVD self-avoidance
191 phenotype for a mutation that disables the actin binding protein, Ena/VASP. We selected
192 Ena/VASP for this test because it has been shown to function as a cytoplasmic effector of actin
193 polymerization downstream of *unc-6/Netrin* signaling [12,29,30]. In addition, the *C. elegans*
194 Ena/VASP homolog, UNC-34 [31], is enriched in a gene expression profile of PVD neurons [11].
195 A strong loss-of-function allele of *unc-34*/Ena/VASP [32] alters overall PVD morphology (e.g.,
196 truncated or misplaced 1°dendrite, fewer 2° branches) (Figure 3B-C, Figure S2A-C). In contrast,

197 mutations in other regulators of actin polymerization (e.g. TIAM-1/Gef, Figure S2D) result in
198 severe truncation of lateral branches including 3° dendrites, a phenotype that points to a role for
199 actin polymerization in dendrite outgrowth [24,25]. PVD neurons in *unc-34* mutant animals show
200 the opposite effect of adjacent 3° dendrites that fail to self-avoid and overgrow one another (Figure
201 3B-C). PVD-specific expression of mCherry-tagged UNC-34 protein rescued this Unc-34 mutant
202 phenotype suggesting that *unc-34* function is cell-autonomous for the self-avoidance response
203 (Figure 3C). *unc-34* mutant 1°and 2° branch defects were not rescued by PVD expression of UNC-
204 34, however, which could be indicative of an additional UNC-34 function in nearby cell types that
205 influence PVD morphogenesis (Figure 3B, Figure S2) [33,34]. Thus, our results suggest that UNC-
206 34/Ena/VASP is selectively required in PVD neurons for dendrite retraction in the self-avoidance
207 response but not for dendrite outgrowth. The previously established role of UNC-34/Ena/VASP
208 as a downstream effector of UNC-5 [20] predicts that *unc-34* should be epistatic to the
209 MYR::UNC-5 gain-of-function phenotype. We confirmed this prediction by showing that the
210 delayed outgrowth PVD dendrites in the PVD::MYR::UNC-5 strain is fully suppressed in *unc-34*
211 mutant backgrounds which display the Unc-34 self-avoidance defect (Figure 3C). This result
212 stands in striking contrast to our finding above that PVD::MYR::UNC-5 is epistatic to the Unc-6
213 self-avoidance phenotype (Figure 2B, C). Thus, our genetic results are consistent with a model in
214 which UNC-6/Netrin acts through UNC-5 to activate UNC-34/Ena/VASP for dendrite retraction
215 in the self-avoidance response.
216
217 For visualizing UNC-34/Ena/VASP in developing dendrites, we labeled UNC-34 with mCherry
218 and co-expressed it in PVD (PVD::mCherry::UNC-34) with LifeAct::GFP to detect actin-
219 containing structures. mCherry::UNC-34 is functional because it rescues the *unc-34* self-

220 avoidance defect (Fig 3C). iSIM super resolution imaging detected punctate mCherry::UNC-34
221 throughout the PVD dendritic array (see Methods) Additional images were collected by AiryScan
222 and TIRF microscopy (Figure S3). Notably, mCherry::UNC-34 puncta are consistently detected
223 at the tips of 3° dendrites (Figure 4A-C, S3), a finding consistent with the observed distal location
224 of Ena/VASP in F-actin containing filopodial structures [35,36]. We used time-lapse imaging to
225 detect potential trafficking of mCherry::UNC-34 (Movie S5). Kymographs as well as particle
226 tracking analysis, detected both mobile and stationary mCherry::UNC-34 puncta in 3° dendrites
227 (Figure 4D-F, S3). These results are consistent with the idea that UNC-34/Ena/VASP is delivered
228 to the tips of 3° dendrites where it mediates actin assembly for branch retraction in the self-
229 avoidance response
230
231 **Mutations that disable actin-polymerizing proteins disrupt dendrite self-avoidance.**
232 Genetic tests of additional regulators of actin polymerization also revealed PVD self-avoidance
233 phenotypes. Lamellipodin (Lpd) interacts with ENA/VASP at the tips of filopodia and
234 lamellopodia to extend actin filaments [12,19]. Mutants of *mig-10*/Lpd display robust PVD self-
235 avoidance defects (Figure 3B, E). Similarly, self-avoidance is disrupted by a mutation that
236 eliminates the Rac GEF activity of UNC-73/Trio, a potent regulator of actin dynamics [15]. The
237 predicted downstream function of UNC-73/Trio in the UNC-5 signaling pathway [27] is confirmed
238 by our finding that the self-avoidance defects of *unc-73/Trio*, like *unc-34/Ena/VASP* mutants, are
239 fully epistatic to the delayed outgrowth phenotype of constitutively active PVD::MYR::UNC-5
240 (Figure 3). We note that both *mig-10*/Lpd and *unc-73*/Trio mutants also show other defects in PVD
241 morphology (e.g., displaced 1° dendrite, fewer 2° branches) (Figure S2) closely resembling those

242 of *unc-34*/Ena/VASP mutants which our results suggest are due to a non-cell autonomous function
243 for UNC-34 (Figure S2).
244 To test for potential roles for branched actin polymerization, we examined a null allele of *wsp-*
245 *1/WASP* (Wiskott-Aldrich Syndrome protein) and observed defective PVD self-avoidance. If *wsp-*
246 *1*/WASP functions in a common pathway with *unc-6*, then the self-avoidance defect of the double
247 mutant, *wsp-1; unc-6*, should be no more severe than that of either *wsp-1* or *unc-6* single mutants.
248 We confirmed this prediction by scoring PVD self-avoidance in *wsp-1; unc-6* mutant animals
249 (Figure 3D). An independent study confirmed the role of *wsp-1* in PVD self-avoidance. This work
250 also reported, however, that *wsp-1* does not enhance the self-avoidance defect of a parallel-acting
251 pathway involving MIG-14/Wntless and thus concluded that *wsp-1* functions downstream of MIG-
252 14/Wntless [37]. Additional experiments are needed to resolve the question of whether WSP-
253 1/WASP functions exclusively in the UNC-6/Netrin vs MIG-14/Wntless self-avoidance pathways.
254
255 Because WASP is known to activate the Arp2/3 complex [14,38], we also performed RNAi knock
256 down of the conserved Arp2/3 component ARX-5/p21 and detected significant PVD self-
257 avoidance defects (Figure 3E). The canonical roles of WASP and the Arp2/3 complex suggest that
258 self-avoidance depends on the formation of branched F-actin networks. Recent studies have shown
259 that actin and actin regulators like TIAM-1/GEF and components of the Wave Regulator Complex
260 (WRC) are required for PVD dendrite outgrowth [26,27] (Figure S2D). Here our genetic results
261 point to the paradoxical idea that elongation and branching of F-actin filaments are also necessary
262 for dendrite retraction and that this mechanism is activated by UNC-6/Netrin in the self-avoidance
263 response.
264

265 **The actin cytoskeleton is highly dynamic in growing and retracting PVD dendrites.**

266 To test the idea that the actin cytoskeleton is differentially modulated for both outgrowth and
267 retraction we expressed LifeAct::GFP in PVD neurons to monitor actin dynamics during dendrite
268 morphogenesis. Although LifeAct::GFP binds both filamentous actin (F-actin) and monomeric G-
269 actin with high affinity, bright LifeAct::GFP-labeled foci typically correspond to F-actin-
270 containing structures [39]. We observed that the LifeAct::GFP signal was consistently brightest
271 nearest the tips of growing dendrites in comparison to internal dendritic regions (Fig. 5B, C) as
272 also reported in other studies [26,27,40]. Time-lapse imaging of PVD::LifeAct::GFP by spinning
273 disk confocal microscopy during the late L3/early L4 stage detected striking, dynamic fluctuations
274 in the LifeAct::GFP signal (Movie S3). We quantified this effect by comparing time-dependent
275 changes in LifeAct::GFP fluorescence versus that of a PVD::mCherry cytosolic marker. The
276 relatively constant intensity of PVD::mCherry signal in these experiments favors the idea that the
277 observed changes in LifeAct::GFP fluorescence could be due to actin dynamics in growing
278 dendrites (Figure 5A, D-E).

279

280 Because genetic knockdown of actin polymerizing proteins (UNC-34/Ena/VASP, MIG-10/Lpd,
281 UNC-73/Trio, WSP-1/WASP, ARX-5/P21) (Figure 3) disrupts self-avoidance and thus suggests
282 that F-actin is required, we monitored the LifeACT::GFP signal at the tips of 3° dendrites during
283 the self-avoidance response (Figure S4) (Movie S3). The cytoplasmic mCherry marker was used
284 to detect contact events as instances in which the measured gap between left and right 3° dendrites
285 approached zero. Although time-lapse imaging detected dynamic fluctuations in LifeAct::GFP
286 fluorescence both before and after contact, we did not observe a quantitative increase in the
287 LifeACT::GFP signal with retraction (Figure S4 and S5). Notably, for these experiments, we used

288 the marker strains (i.e., PVD::LifeAct::GFP and PVD::mcherry), imaging strategy (i.e., 40 X
289 objective, 35 s sampling interval) and method of quantitative analysis described in an earlier
290 publication that reported increased LifeAct::GFP fluorescence after contact (N = 14, p = 0.54, two-
291 way ANOVA with Bonferroni correction [37] (Figure S4A-C). In an additional approach, we used
292 a higher resolution objective (100X) and longer sampling interval (1 – 1.3 min) and also did not
293 detect elevated LifeAct::GFP fluorescence during retraction (N = 8, p = 0.74, two-way ANOVA
294 with Bonferroni correction) (Figure S4D and S5). The simplest explanation of our results is that
295 actin polymerization drives both outgrowth and retraction which are tightly coupled over time at
296 dendrite tips and thus difficult to resolve as separate events.
297
298 **NMY-1/Non-muscle myosin II drives dendrite retraction in the self-avoidance mechanism.**
299 Our imaging results indicate that F-actin is the dominant cytoskeletal structure in growing PVD
300 dendrites. In considering a mechanism to account for dendrite shortening in the self-avoidance
301 response, we hypothesized that a newly synthesized actin cytoskeleton could mediate dendrite
302 shortening by providing a substrate for non-muscle myosin II to drive contraction. To test this
303 idea, we examined loss-of-function alleles that disable the *C. elegans* non-muscle myosins, NMY-
304 1 and NMY-2. This experiment determined that mutations in *nmy-1* but not *nmy*-2 [40] show PVD
305 self-avoidance defects (Figure 6). This effect is cell autonomous for *nmy-1* because PVD-specific
306 RNAi of *nmy-1* also results in overlapping 3° dendrites and PVD-specific expression of GFP-
307 tagged NMY-1 is sufficient to rescue the *nmy-1* self-avoidance defect (Figure 6 B-D). We conclude
308 that a specific non-muscle myosin, NMY-1, promotes dendrite retraction in the self-avoidance
309 mechanism and could act by driving the translocation of F-actin bundles at the tips of 3° dendrites.
310

311 **Phosphomimetic activation of MLC-4 shortens PVD 3° dendrites.**

312 Non-muscle myosin II motor proteins are composed of myosin heavy chain (MHC) and light
313 chains, the essential light chain (ELC) and regulatory light chain (RLC) [41,42]. Myosin motor
314 activity is triggered by RLC phosphorylation that induces a conformational change to allow
315 assembly of the myosin complex into active bipolar filaments (Figure 7A) [43]. Having shown
316 that NMY-1/non-muscle myosin is required for self-avoidance, we next performed an additional
317 experiment to ask if constitutive non-muscle myosin activity is sufficient to induce dendrite
318 retraction. For this test, we expressed a phosphomimetic mutant of MLC-4, the *C. elegans* RLC
319 homolog. MLC-4/myosin regulatory light chain contains serine/S and threonine/T phosphorylation
320 sites in a highly-conserved domain. Both S and T residues were mutated to Aspartate/D and the
321 resultant phosphomimetic construct MLC-4DD was fused to GFP for transgenic expression in
322 PVD (Figure 7B-C) [44]. PVD neurons that expressed MLC-4DD showed significantly shorter 3°
323 dendrites at the L3 stage in comparison to wild type as well as a concurrent increase in the width
324 of gaps between 3° dendrites from adjacent menorahs (Figure 7D-G). These phenotypic traits are
325 consistent with the idea that normal dendrite outgrowth is slowed by constitutive activation of non-
326 muscle myosin by MLC-4ADD. By the L4 stage, PVD architecture in the MLC-4DD strain
327 resembles that of the wild type with normal appearing menorah morphology and spacing (Figure
328 8A, B). Similar results were observed for PVD neurons that express constitutively active
329 MYR::UNC-5 which we have proposed functions downstream of UNC-6/Netrin to trigger the self-
330 avoidance response (Figure 2). Our finding that MLC-4DD rescues the self-avoidance defect of
331 *unc-6* mutants suggests that NMY-1/non-muscle myosin II also functions downstream of *unc-6*
332 for dendrite retraction (Figure 8C).

333

334 **Antagonistic pathways regulate dendrite outgrowth vs self-avoidance.**

335 Our time lapse imaging studies detected dynamic actin polymerization in growing PVD dendrites
336 (Movie S3). This observation and the recent finding that PVD dendrites are truncated and
337 misdirected by mutations that disable either a specific actin structural gene, *act-4*, or specific
338 components (WRC and TIAM/GEF) that promote actin polymerization, suggest that dendritic
339 outgrowth depends on actin assembly [26,27] (Figure S2D). Actin assembly is also likely required
340 for dendrite retraction given results showing that genetic knockdown of a separate set of actin-
341 binding proteins (i.e., UNC-34/Ena/VASP, MIG-10/Lpd, UNC-73/Trio, WSP-1/WASP, ARX-
342 5/p21) (**Fig. 3**), blocks PVD self-avoidance but not dendrite outgrowth [37]. A shared role for
343 actin polymerization in both outgrowth and retraction argues that the net length of PVD dendrites
344 must depend on an intrinsic mechanism that regulates actin assembly to balance these competing
345 effects.

346

347 Our results suggest that UNC-6/Netrin signaling promotes dendrite retraction in a mechanism
348 involving F-actin assembly. PVD dendritic outgrowth is driven by a separate pathway in which
349 DMA-1, a membrane protein expressed in PVD, interacts with a multicomponent receptor
350 anchored in the adjacent epidermis [13,45-49]. Dendritic growth depends on binding of DMA-1
351 and the claudin-like protein, HPO-30, to specific regulators of actin assembly (i.e., WAVE
352 regulatory complex, TIAM-1/GEF) in the PVD cytoplasm [26,27,50]. These interactions may be
353 modulated by the Furin KPC-1 which antagonizes DMA-1 surface expression in PVD [45-47].
354 *kpc-1* activity is proposed to temporally weaken adhesion with the epidermis to facilitate changes
355 in trajectory at specific stages in dendritic outgrowth [47,48]. For example, the tips of 3° branches
356 typically execute a right-angle turn after the self-avoidance response to produce a 4° dendrite [11].

357 This morphological transition largely fails in *kpc-1* mutants in which 3° dendrites elongate
358 abnormally and show severe self-avoidance defects due to over-expression of DMA-1 [47,48].
359 Thus, we considered the idea that self-avoidance is achieved by the combined effects of *kpc-1*-
360 dependent downregulation of DMA-1 and a separate mechanism that antagonizes outgrowth and
361 requires UNC-6/Netrin. We performed a series of genetic experiments to test this model.
362
363 The hypomorphic loss-of-function allele, *kpc-1(xr58),* results in over-expression of DMA-1 and a
364 consequent, robust self-avoidance defect with ~42% of sister 3° branches overlapping one another
365 (Figure 9A, D) [46,47]. This defect is not observed, however, in *kpc-1*/+ heterozygotes (Figure
366 9D). Similarly, self-avoidance in *unc-6*/+ heterozygous animals is indistinguishable from wild
367 type (Figure 9D). Thus, a 2-fold reduction in gene dosage for either *kpc-1* or *unc-6* does not perturb
368 self-avoidance. We reasoned, however, that if expression of UNC-6/Netrin and KPC-1 were
369 simultaneously reduced by half, then self-avoidance should be at least partially disabled since both
370 *unc-6* and *kpc-1* normally function to antagonize dendrite outgrowth. To test this prediction, we
371 constructed double heterozygous mutants of *kpc-1* and *unc-6* (e.g., *kpc-1*/+*; unc-6*/+) and
372 quantified the self-avoidance phenotype. This experiment revealed that ~30% of adjacent sister 3°
373 dendrites fail to self-avoid in *kpc-1*/+*; unc-6*/+ animals which is significantly greater than that of
374 either *kpc-1*/+ or *unc-6*/+ single mutants (Figure 9B, D). This genetic "enhancer" effect is
375 consistent with the idea that both KPC-1 and UNC-6 function to limit growth of 3° dendrites. If
376 this effect is due to elevated levels of DMA-1 arising from reduced KPC-1 activity in the *kpc-1*/+*;*
377 *unc-6*/+ background, then a concomitant diminution of DMA-1 activity should restore normal self-
378 avoidance. We tested this idea by constructing the triple heterozygote, *kpc-1* +/+ *dma-1; unc-6*/+,
379 and detected robust suppression of the self-avoidance defect observed in *kpc-1*/+*; unc-6*/+ animals

380 (Figure 9C, D). Thus, these results suggest that DMA-1-mediated adhesion to the epidermis
381 antagonizes UNC-6/Netrin-dependent dendrite retraction and that the relative strengths of these
382 opposing pathways must be finely tuned to achieve the self-avoidance effect (Figure 9E). The key
383 role of actin polymerization in both UNC-6/Netrin-mediated retraction and DMA-1-dependent
384 outgrowth argues that this balancing mechanism likely regulates both modes of actin assembly.

385 **DISCUSSION**

386

387 Dendrites arising from the same neuron typically do not overlap. This phenomenon of dendrite
388 self-avoidance is universally observed and derives from an active mechanism in which contact
389 between sister dendrites triggers mutual retraction [4,48]. As might be predicted for an event that
390 depends on physical proximity, cell-surface associated proteins have been shown to mediate
391 dendrite self-avoidance [37,49]. These include Dscam and protocadherins which are expressed in
392 multiple alternative forms to distinguish self from non-self among contacting dendrites [5-7]. Self-
393 avoidance for certain neurons can also depend on the interaction of diffusible cues with their
394 cognate receptors [8,49]. For example, we have shown that the axon guidance signal, UNC-
395 6/Netrin, and its receptors, UNC-5 and UNC-40/DCC, function together to mediate self-avoidance
396 for PVD sensory neurons in *C. elegans*. We have proposed that UNC-40/DCC captures UNC-
397 6/Netrin on the membrane surface to facilitate repulsion through physical interaction with UNC-5
398 on PVD dendrites [9] (Figure S1D). Little is known, however of the downstream effectors of
399 dendrite retraction in the self-avoidance response. Here we report new results that are consistent
400 with a model in which UNC-6/Netrin promotes actin-polymerization to propel dendrite retraction.
401 Our finding that non-muscle myosin is also involved resolves the paradoxical idea that UNC-
402 6/Netrin-dependent actin polymerization shortens rather than lengthens PVD 3° dendrites. We
403 propose that non-muscle myosin engages the F-actin cytoskeleton at the tips of PVD dendrites to
404 drive retraction.

405

406 **Regulators of actin polymerization are required for dendrite self-avoidance.**

407 The proposed role for actin polymerization in the self-avoidance response derives from our finding
408 that multiple regulators of F-actin assembly are necessary for efficient dendrite retraction. For
409 example, a mutation that disables UNC-34, the *C. elegans* homolog of Ena/VASP, disrupts PVD
410 self-avoidance. Ena/VASP promotes actin polymerization by preventing capping proteins from
411 blocking the addition of actin monomers to the plus-end of elongating actin filaments. In axon
412 growth cones, Ena/VASP localizes to the tips of actin bundles in growing filopodia [12,36]. We
413 observed punctate Ena/VASP localization at the tips of PVD dendrites and active trafficking from
414 the cell soma (Figures 4 and S3). Our results showing that an *unc-34* mutant suppresses the
415 retarded dendrite outgrowth phenotype arising from the constitutively active MYR::UNC-5
416 (Figure 3) argues that *unc-34* functions downstream to mediate UNC-6/Netrin-dependent self-
417 avoidance. Additional genetic evidence indicates that WSP-1/WASP also acts in a common
418 pathway with UNC-6/Netrin (Figure 3). The established role for WASP of activating the Arp2/3
419 complex [50] is consistent with our finding that RNAi knockdown of *arx-5/p21*, a conserved
420 Arp2/3 component, partially disables the self-avoidance mechanism (Figure 3). Dual roles for
421 UNC-34 and WSP-1 in actin polymerization, as suggested here, are consistent with previous work
422 indicating that Ena/VASP can activate Arp2/3 through direct interaction with WASP proteins
423 [31,51-53]. Thus, taken together, our results suggest that Ena/VASP and WSP-1 coordinate the
424 creation of branched actin networks at the tips of retracting PVD dendrites in the UNC-6/Netrin
425 dependent self-avoidance response (Figure 9E).
426
427 A role for Ena/VASP in dendrite retraction, as have we have proposed here, parallels earlier
428 findings of a necessary function for Ena/VASP in growth cone repulsion. For example, axon
429 guidance defects arising from ectopic expression of UNC-5 in *C. elegans* touch neurons requires

430 UNC-34/Ena/VASP [54], a finding confirmed by our observation that the dendritic shortening
431 phenotype induced by MYR::UNC-5 is prevented by a loss-of-function mutation in *unc-34*.
432 Ena/VASP is also required for axon repulsion mediated by Slit and its receptor Robo [20,55,56].
433 Although Ena/VASP function can be readily integrated into models of axonal attraction, the well-
434 established role of Ena/VASP in F-actin assembly has been more difficult to rationalize in
435 mechanisms of axonal repulsion which are presumed to involve actin depolymerization [12,57]. A
436 partial explanation for this paradox is provided by a recent study showing that Slit, acting through
437 Robo, induces transient filopodial outgrowth in migrating axonal growth cones and that this effect
438 requires Ena/VASP [56]. The functional necessity for filopodial growth in this mechanism is
439 unclear, but the central role of Ena/VASP-induced actin assembly in the overall repulsive response
440 to Slit mirrors our results suggesting that dendrite retraction in PVD neurons requires UNC-
441 34/Ena/VASP and F-actin assembly.
442
443 Our studies also detected necessary roles in self-avoidance for MIG-10/LPD which has been
444 previously shown to function with UNC-34/Ena/VASP to promote F-actin polymerization and
445 UNC-73/Trio, a Rho/Rac GEF that acts in UNC-6/Netrin pathways to regulate the actin
446 cytoskeleton [15,19,20,27]. Altogether, our genetic analysis identified five known effectors of
447 actin polymerization (UNC-34/Ena/VASP, WSP-1/WASP, Arp2/3 complex, MIG-10/Lpd, UNC-
448 73/Trio) that mediate the self-avoidance response but which are not required for 3° branch
449 extension during outgrowth (Figure 3, S2).
450
451 **Non-muscle myosin II mediates dendrite retraction in the self-avoidance response.**

452 Our genetic analysis detected a cell-autonomous role for NMY-1/non-muscle myosin II in dendrite
453 self-avoidance (Figure 6). Because our results revealed F-actin at the tips of PVD dendrites (Figure
454 5), we suggest that NMY-1 mediates retraction by interacting with F-actin to drive a contractile
455 mechanism. For example, NMY-1 could accelerate retrograde flow, a non-muscle myosin-
456 dependent effect that also drives filopodial retraction in growth cones and at the leading edge of
457 migrating cells [58,59]. Alternatively, NMY-1 could shorten PVD dendrites by inducing the
458 reorganization of the nascent actin cytoskeleton into a more compact structure [60].
459 Phosphorylation of myosin regulatory light chain (RLC) activates non-muscle myosin [43] and we
460 showed that MLC-4DD, a phosphomimetic, and, thus, constitutively active form of the *C. elegans*
461 homolog of RLC, results in delayed outgrowth of PVD 3° dendrites (Figure 7). The retarded
462 dendrite outgrowth resulting from chronic activation of MLC-4 suggests a model in which NMY-
463 1 function is triggered by contact between sister dendrites and subsequent UNC-6/Netrin signaling.
464 A downstream function for non-muscle myosin II in the UNC-6/Netrin pathway is consistent with
465 our finding that the Unc-6 self-avoidance defect is rescued by MLC- 4DD (Figure 8). Parallel
466 roles for these components in axon guidance are suggested by recent results showing that non-
467 muscle myosin II is required for Slit and Netrin-dependent midline avoidance in the developing
468 vertebrate spinal cord [61]. Similarly, non-muscle myosin II mediates Semaphorin-induced axonal
469 repulsion. The mechanism of Semaphorin action in this case also involves the assembly of actin
470 bundles in the axon shaft presumably to facilitate non-muscle myosin-driven retraction [62-64].
471 Thus, our findings suggest that key drivers of axonal repulsion including nascent actin assembly
472 and non-muscle myosin may also mediate dendrite retraction in the self-avoidance response.
473

474 RLC phosphorylation activates non-muscle myosin II by releasing myosin monomers for assembly
475 into bipolar structures or myosin "stacks" that interact with actin filaments to induce translocation
476 [43,65]. Although our results are consistent with a necessary role for non-muscle myosin in
477 dendrite retraction, the tips of PVD 3° dendrites are likely too narrow (~50 nm) [10] to
478 accommodate myosin stacks (~300 nm) [65,66]. We suggest that the actin-branching function of
479 Arp2/3, which we have shown mediates PVD dendrite retraction, could induce transient expansion
480 of the dendritic tip to allow assembly of myosin stacks. In this model, actin-polymerization
481 involving Arp2/3 could effectively limit ectopic NMY-1 activation in the dendritic shaft by
482 restricting the assembly of myosin stacks to the tips of contacting sister dendrites. Alternatively,
483 recent evidence indicates that myosin can also induce contraction in its monomeric or
484 unpolymerized form [67] which should have ready access to the dendrite tip. This idea is consistent
485 would our observation that GFP-tagged NMY-1 is active (e.g., rescues the self-avoidance defect
486 of *nmy-1*) and did not display the punctate appearance characteristic of myosin stacks [65] but is
487 diffusely localized throughout the PVD cytoplasm (Figure 6B).
488
489 **Parallel-acting pathways regulate dendrite self-avoidance.**
490 Although self-avoidance is perturbed in UNC-6/Netrin pathway mutants, a significant fraction
491 (~70%) (Figure 3D) of PVD 3° dendrites show apparently normal self-avoidance behavior [9].
492 One explanation for this observation is provided by the recent discovery of an independent
493 pathway, mediated by MIG/14/Wntless, that is necessary for self-avoidance in an additional
494 fraction of PVD 3° dendrites [37]. Parallel acting pathways also mediate self-avoidance in
495 mammalian Purkinje neurons where slit-robo signaling acts in concert with protocadherins [6,8].
496 The likelihood of additional effectors of self-avoidance is also suggested by the incompletely

497 penetrant effects of Dscam mutants in Drosophila sensory neuron self-avoidance [68]. Thus, our
498 results in *C. elegans* mirror findings in other organisms which together suggest that multiple
499 mechanisms have evolved to insure dendrite self-avoidance.
500
501 **The actin cytoskeleton is highly dynamic in growing and retracting PVD dendrites.**
502 We used time-lapse imaging with LifeAct::GFP, a live-cell marker for actin {Riedl:2008gw}, to
503 monitor actin PVD dendrites. The LifeAct::GFP signal is typically brighter near the distal ends of
504 growing branches in comparison to interstitial regions (Figure 5) and is highly dynamic (Movie
505 S3). The distal localization and rapidly fluctuating LifeAct::GFP signal in PVD dendrites
506 resembles recently reported "actin blobs" that actively migrate in highly branched Drosophila
507 sensory neurons where they appear to presage points of branch initiation [69]. A strong
508 LifeAct::GFP signal at the tips of emerging PVD dendrites is also consistent with genetic evidence
509 that actin polymerization is required for dendrite outgrowth [24,25]. Although our genetic results
510 (Figure 3) suggest a model of dendrite retraction in which nascent actin polymerization is
511 necessary for the self-avoidance response, our measurements did not detect a quantitative increase
512 in LifeAct::GFP in retracting vs growing 3° dendrites as previously reported by others [37]. This
513 result suggests that the overall level of actin polymerization is high during both outgrowth and
514 retraction but may be incorporated into distinct structures, regulated by distinct groups of effectors
515 (see below) that our imaging methods do not resolve.
516
517 **Antagonistic pathways regulate dendrite outgrowth vs retraction.**
518 Dendritic architecture is defined by the combined effects of outgrowth which expands the arbor vs
519 retraction which limits the size of the receptive field. This interaction of positive and negative

520 effects is readily observed in the development of 3° PVD dendrites. Initially, 3° dendrites
521 emanating from adjacent menorahs grow out along the body axis until contacting one another and
522 then retract to avoid overlap [9,11]. Outgrowth in this case is promoted by a multicomponent
523 receptor-ligand complex that mediates adhesive interactions with the adjacent epidermis [70-73]
524 (Figure 9E). When this pathway is dysregulated by over-expression of the DMA-1 receptor in
525 PVD neurons, for example, 3° dendrites continue to adhere to the epidermis and overgrow one
526 another [47,74]. 3° branch self-avoidance also fails in mutants that disable UNC-6/Netrin signaling
527 which we have shown promotes dendrite retraction [9]. Thus, these results suggest that the net
528 length and placement of each 3° branch depends on the balanced effects of locally acting signals
529 that either extend (e.g., DMA-1) or shorten (e.g., UNC-6/Netrin) the dendrite. We confirmed this
530 idea in genetic experiments that detected strong dose-sensitive interactions between these opposing
531 pathways. For example, a 50% reduction of UNC-6/Netrin expression in a heterozygous *unc-6*/+
532 mutant does not perturb self-avoidance. Similarly, a genetic mutant (*kpc-1*/+) that partially
533 elevates DMA-1 also shows normal 3° branch outgrowth. The combination of both mutations in
534 the double heterozygote, *unc-6*/+; *kpc-1*/+, however, produces a strong self-avoidance defect
535 (Figure 9). Our genetic results identified multiple regulators of actin polymerization (UNC-
536 34/Ena/VASP, WSP-1/WASP, ARX-5/p21, MIG-10/Lamelipodin, UNC-73/Trio) that are
537 required for self-avoidance (Figure 3). We thus propose that UNC-6/Netrin promotes actin
538 polymerization to effect dendrite retraction and that non-muscle myosin II interacts with a nascent
539 actin cytoskeleton to translocate each 3° dendrite away from its neighbor. F-actin is also abundant
540 and highly dynamic in growing PVD dendrites. Notably, a distinct set of F-actin promoting factors
541 (WRC, TIAM/GEF) interacts with the DMA-1 receptor complex to drive PVD dendritic growth
542 (Figure 9E) [26,27]. Additional genetic evidence suggests that the WRC could also function in

543 self-avoidance [37]. Thus, the challenge for future studies is to elucidate the cell biological
544 machinery through which opposing pathways manipulate the actin cytoskeleton to effect either
545 dendrite growth or retraction.
546

547 **MATERIALS AND METHODS**

548

549 **Strains and genetics**

550 All the strains used were maintained at 20°C and cultured as previously described (Brenner, 1974).

551 We used the N2 Bristol strain as wild-type.

552

553 Additional strains used in this study: NC1404 [*wdIs52* (*pF49H12.4*::GFP)], NW434 [*unc-*

554 *6(ev400)X*;*wdIs52(pF49H12.4::GFP)*], TV17,200 [*kpc-1(xr58); wyIs592(pser2prom3::GFP)*]

555 [47], TV9656 [*dma-1(wy686); unc-119(ed3)III; wyEx3355(pser2prom3::GFP+odr-1::RFP)*],

556 CX1248 [*KyEx3482*(*pdes-2::TBA-1::mCherry+coel::RFP*)] {Maniar:2011gx}, CLP928

557 [*twnEx382(Pser2.3::LifeAct::EGFP, Pser2.3::mCherry, Pgcy-8::gfp)*] [37].

558

559 Additional strains generated for this study: NC2580 *unc-34(gm104)V*; *wdIs52*, NG324 [*wsp-*

560 *1(gm324)*; *wdIs52*], *+/szT1 lon-2(e678) I;* HR1184 [*nmy-1(sb115) dpy-8(e130)/szT1 X*], NC2726

561 [*nmy-1(sb113)*;*wdIs52*], *unc-73(rh40)*]; *wdIs52*.

562 NC3284 [*wdEx1011* (*pF49H12.4*::myrUNC-5::GFP)], was produced by microinjection of

563 plasmids pLSR18 (*pF49H12.4*::myrUNC-5::GFP), *pmyo-2*::mCherry and pCJS04

564 (*pF49H12.4*::mCherry).

565 NC3048 [*wdIs98* (*pF49H12.4*::ACT-1::GFP)] was produced by microinjection of plasmids

566 pLSR03 (*pF49H12.4*::ACT-1::GFP) and *pceh-22*::GFP and integrated as previously described

567 (Miller and Niemeyer, 1995).

568 NC3085 [*wdEx967* (*pF49H12.4*::mCherry::UNC-34)] was obtained by microinjection of plasmids

569 pCJS78(*pF49H12.4*::mCherry::UNC-34) and *pmyo-2*::mCherry.

570 NC3090 [*wdEx972* (*pF49H12.4*::LifeAct::GFP)] was acquired by microinjecting plasmids
571 pLSR06 (*pF49H12.4*::LifeAct::GFP) and *pmyo-2*::mCherry.
572 NC3029 [(*pF49H12.4*::*nmy-1(+)* + *pF49H12.4*::*nmy-1(-)*)] was obtained by microinjection of
573 pLSR09 (*pF49H12.4*::*nmy-1(+)*), pLSR10 (*pF49H12.4*::*nmy-1(-)*), pmyo-2::mCherry and
574 pCJS04 (*pF49H12.4*::mCherry)
575 NC3087 [*wdEx969* (*pF49H12.4*::GFP::Linker::NMY-1)] was produced by microinjecting
576 plasmids pLSR11 (*pF49H12.4*::GFP::Linker::NMY-1), pCJS04 (*pF49H12.4*::mCherry) and
577 pmyo-2::mCherry.
578 *wdEx1009* (*pF49H12.4*::GFP::Linker::MLC-4DD) [NC3283] was obtained by microinjection of
579 plasmids pLSR17 (*pF49H12.4*::GFP::Linker::MLC-4), pCJS04 (*pF49H12.4*::mCherry) and
580 *pmyo-2*::mCherry**.**
581
582 **Molecular Biology**:
583 **pLSR11 (*pF49H12.4::*GFP::Linker::NMY-1::*unc-10* 3'UTR):** We used the Clonetech in-
584 fusion HD cloning kit (Cat # 638910) to build this plasmid. The *nmy-1* genomic region was
585 amplified from pACP01 (*pF49H12.4::*NMY-1::mCherry) with overlapping regions
586 corresponding to pCJS95 (*pF49H12.4::*GFP::CED-10::*unc-10* 3'UTR). We also PCR amplified
587 pCJS95 with primers overlapping the *nmy-1* genomic sequences to swap CED-10 with NMY-1.
588 We then used the NEB site-directed mutagenesis kit to insert a 24-nucleotide glycine rich linker
589 (see Table 1) [65]. The resultant pLSR11 plasmid was sequenced to confirm that the linker was
590 inserted between the GFP sequence and *nmy-1*. See table 1 for primer sequences.
591

592 **Constructing pLSR17 (*pF49H12.4*::GFP::Linker::MLC-4DD):** We used the Clonetech in-
593 fusion HD cloning kit (Cat # 638910) to construct this plasmid. The *mlc-4* genomic region was
594 amplified from wild-type (N2) DNA using primers with overlapping adapters complementary to
595 pLSR11 (*pF49H12.4*::GFP::Linker::NMY-1). pLSR11 was amplified with primers containing
596 adapter sequences complementary to *mlc-4*. The amplified fragments were combined for the
597 infusion cloning to replace *nmy-1* with *mlc-4*. We then used the NEB site directed mutagenesis
598 kit to change MLC-4 codons for Serine 18 and Threonine 17 to nucleotide sequences that encode
599 aspartatic acid (D). The resultant pLSR17 plasmid was confirmed by sequencing.
600
601 **Confocal microscopy and image analysis**: Animals were immobilized with 15 mM levamisole/
602 0.05% tricaine and mounted on 2% agarose pads in M9 buffer as previously described [11]. Z
603 stack images were collected using a Nikon TiE inverted fluorescent microscope equipped with an
604 A1R point scanning confocal and a Plan Apo 40X, 1.3NA oil immersion objective or on a Leica
605 TCS SP5 confocal microscope with a 40X or 63X objective. Z stacks were collected at either 0.5
606 or 1μm depth from the position of ventral nerve cord to the top of PVD cell body. Maximum
607 projection images were collated with either LAS-AF (Leica) or with NIS elements software
608 (Nikon). Dendrite length was measured using the line tool in Fiji/image J. Co-localization images
609 were assembled using image J. Z stack images that were collected using the LAS-AF or NIS
610 elements software was imported into ImageJ/Fiji for further analysis.
611
612 **iSIM super-resolution imaging and analysis**. Animals were immobilized with 0.4 mM
613 levamisole and mounted on 10% agarose pads in M9 buffer. Z stack images were captured using
614 a Hamamatsu sCMOS camera on a iSIM microscope (VisiTech International) equipped with a

615 100X, 1.45 NA objective. Images were deconvolved and processed using Metamorph and
616 Fiji/ImageJ.
617
618 **Imaris software image analysis**. Time-lapse movies from the iSIM microscope were
619 deconvolved with metamorph. The spot tracking algorithm (Imaris) was used to track UNC-
620 34::mCherry particles of minimum diameter of 0.3 μm. Displacement refers to the distance (μm)
621 between the location of an UNC-34::mCherry particle at a given time versus its starting position
622 at t = 0.
623
624 **Spinning disk confocal microscopy:** Animals were immobilized with 0.4mM levamisole and
625 mounted on 10% agarose pads in M9 buffer. Volumes over time were captured using an automated
626 TiE inverted fluorescence microscope platform with an X1 spinning disk head (Yokogawa) and
627 DU-897 EM-CCD (Andor Technology), piezo-electric Z stage (Mad City Labs) and Apo TIRF
628 100x 1.49 NA oil immersion objective (Nikon Instruments, Inc.). Analysis of fluorescence
629 intensity was accomplished using NIS-Elements and Fiji/Image J software.
630
631 **Quantification of fluorescence intensity in growing vs. non-growing dendrites:** L2-L3 larvae
632 were immobilized with 0.4mM levamisole and mounted on 10% agarose pads in M9 buffer for
633 imaging with the spinning disk confocal microscope. Z-stacks of PVD dendrites were imaged at
634 either 1 min or 1.30 minute intervals with the 100X 1.49 NA oil immersion objective. PVD
635 dendrites (2º, 3º and 4º) undergoing outgrowth with a succession of rapid extensions and
636 retractions during the length of the time lapse videos were analyzed. NIS elements was used for
637 measurements of LifeAct::GFP from a 1μm ROI at the tips of growing dendrites. In the same

638 videos, fluorescence intensity was measured for an identical 1μm ROI of PVD branches (1º, 2º
639 and 3º) that were not undergoing outgrowth. Fluorescence intensity measurements for the
640 outgrowth and no-outgrowth datasets were normalized against the maximum overall LifeAct::GFP
641 value (Figure 5).
642
643 **Statistics:** Student's t test was used for comparisons between 2 groups and ANOVA for
644 comparisons between three or more groups with either Tukey posthoc or Bonferroni correction for
645 multiple comparisons. Kolmogorov-Smirnov test was performed for comparisons between
646 frequency distributions of 3° dendrite length and gaps between 3° dendrites (Figures 2C and 8F,
647 G) .
648
649 Table 1.
650

Primer name	Primer sequences
myrunc-5 Vec. For.	CGGCCGCGGATAACAAATTTCA
myrunc-5 Vec. Rev.	GGATCCCATCCCGGGGAT
myrunc-5 Frag. For.	CCCGGGATGGGATCCATGggatcttctaagtctgctagcAAAC
myrunc-5 Frag. Rev.	TGTTATCCGCGGCCGCTATTTGTATAGTTCATCCATGCCATGTG
nmy-1 linker F1	GGATGCCCCTCCgtacagctcgtccatg
nmy-1 linker R1	GCAGGGGGAGGTGATGGGTGACCTGCAGTAC
mlc-4DD F1	CATGTTCGATCAGGCTCAAATTCAAG
mlc-4DD R1	GCGAACACATTGTCATCGGCTCTTTG
mlc-4 Vec. For.	GGATAACAAATTTCTATGTTTTTGTTTGTTTTTTGTCTTAATTACCA

mlc-4 Vec. Rev.	ACCTCCCCCTGCGGATG
mlc-4 Frag. For.	TCCGCAGGGGGAGGTATGGCCTCCCGCAAAACC
mlc-4 Frag. Rev.	agaaatttgttatccTTAAGCCTCATCCTTGTCCTTGGTTCC

651
652
653
654
655

656 **ACKNOWLEDGMENTS**

657

658 We thank C. Bargmann, K. Shen, J. Plastino, Dr. T.J. Kubiseski, E. Lundquist, P. Mains and H.
659 Buelow for strains and reagents. We thank Chun-Liang Pan and Chien-Po Liao for sharing their
660 work, reagents and advice prior to publication, Dylan Burnette and members of his laboratory,
661 Aidan Fenix and Nilay Taneja, for helpful suggestions and members of the Miller lab for comments
662 on the manuscript. Spinning disk images were obtained in the Nikon Center of Excellence at
663 Vanderbilt University. We thank Fernando Delaville and Ralph Bauer from BioVision
664 Technologies for their help in acquiring time-lapse movies and images on the iSIM microscope.
665 This work was supported by NIH Grants R01 NS079611 to D. M. M, F31 NS071801 to C.J.S and
666 F31 NS49743 to J. D. W. Some of the strains used in this work were provided by the *C.*
667 *elegans* Genetics Center, which is supported by the US National Institutes of Health (NIH)
668 National Center for Research Resources. L.S., C.J.S and J.D.W. performed experiments with
669 advice from D.M.M., M.J.T. provided imaging expertise and advice; B.A.M helped with spinning
670 disk imaging and edited videos, L.S. and D.M.M. wrote the paper with input from coauthors.

671

672 **REFERENCES**

673 1. Delandre C, Amikura R, Moore AW. Microtubule nucleation and organization in
674 dendrites. cc. 2016;15: 1685–1692. doi:10.1080/15384101.2016.1172158

675 2. Jan YN, Jan LY. Branching out: mechanisms of dendritic arborization. Nat Rev
676 Neurosci. 2010;11: 316–328. doi:10.1038/nrn2836

677 3. Konietzny A, Bär J, Mikhaylova M. Dendritic Actin Cytoskeleton: Structure,
678 Functions, and Regulations. Front Cell Neurosci. 2017;11: 147.
679 doi:10.3389/fncel.2017.00147

680 4. Grueber WB, Sagasti A. Self-avoidance and tiling: Mechanisms of dendrite and
681 axon spacing. Cold Spring Harb Perspect Biol. 2010;2: a001750–a001750.
682 doi:10.1101/cshperspect.a001750

683 5. Fuerst PG, Bruce F, Tian M, Wei W, Elstrott J, Feller MB, et al. DSCAM and
684 DSCAML1 function in self-avoidance in multiple cell types in the developing
685 mouse retina. Neuron. 2009;64: 484–497. doi:10.1016/j.neuron.2009.09.027

686 6. Lefebvre JL, Kostadinov D, Chen WV, Maniatis T, Sanes JR. Protocadherins
687 mediate dendritic self-avoidance in the mammalian nervous system. Nature. Nature
688 Publishing Group; 2012;488: 517–521. doi:10.1038/nature11305

689 7. Matthews BJ, Kim ME, Flanagan JJ, Hattori D, Clemens JC, Zipursky SL, et al.
690 Dendrite self-avoidance is controlled by Dscam. Cell. 2007;129: 593–604.
691 doi:10.1016/j.cell.2007.04.013

692 8. Gibson DA, Tymanskyj S, Yuan RC, Leung HC, Lefebvre JL, Sanes JR, et al.
693 Dendrite Self-Avoidance Requires Cell-Autonomous Slit/Robo Signaling in
694 Cerebellar Purkinje Cells. Neuron. Elsevier Inc; 2014;81: 1040–1056.
695 doi:10.1016/j.neuron.2014.01.009

696 9. Smith CJ, Watson JD, Vanhoven MK, Colón-Ramos DA, Miller DM III. Netrin
697 (UNC-6) mediates dendritic self-avoidance. Nat Neurosci. 2012;15: 731–737.
698 doi:10.1038/nn.3065

699 10. Albeg A, Smith CJ, Chatzigeorgiou M, Feitelson DG, Hall DH, Schafer WR, et al.
700 C. elegans multi-dendritic sensory neurons: morphology and function. Mol Cell
701 Neurosci. 2011;46: 308–317. doi:10.1016/j.mcn.2010.10.001

702 11. Smith CJ, O'Brien T, Treinin M, Miller DM III. Time-lapse imaging and cell-
703 specific expression profiling reveal dynamic branching and molecular determinants
704 of a multi-dendritic nociceptor in C. elegans. Developmental Biology. 2010;345:
705 18–33. doi:10.1016/j.ydbio.2010.05.502

706 12. Drees F, Gertler FB. Ena/VASP: proteins at the tip of the nervous system. Current
707 Opinion in Neurobiology. 2008;18: 53–59. doi:10.1016/j.conb.2008.05.007

708 13. Goley ED, Welch MD. The ARP2/3 complex: an actin nucleator comes of age. Nat
709 Rev Mol Cell Biol. 2006;7: 713–726. doi:10.1038/nrm2026

710 14. Takenawa T, Suetsugu S. The WASP-WAVE protein network: connecting the
711 membrane to the cytoskeleton. Nat Rev Mol Cell Biol. 2007;8: 37–48.
712 doi:10.1038/nrm2069

713 15. Steven R, Kubiseski TJ, Zheng H, Kulkarni S, Mancillas J, Ruiz Morales A, et al.
714 UNC-73 activates the Rac GTPase and is required for cell and growth cone
715 migrations in C. elegans. Cell. 1998;92: 785–795.

716 16. Hu S, Pawson T, Steven RM. UNC-73/Trio RhoGEF-2 Activity Modulates
717 Caenorhabditis elegans Motility Through Changes in Neurotransmitter Signaling
718 Upstream of the GSA-1/G s Pathway. Genetics. 2011;189: 137–151.
719 doi:10.1534/genetics.111.131227

720 17. Matsuo N, Hoshino M, Yoshizawa M, Nabeshima Y-I. Characterization of STEF, a
721 guanine nucleotide exchange factor for Rac1, required for neurite growth. J Biol
722 Chem. 2002;277: 2860–2868. doi:10.1074/jbc.M106186200

723 18. Demarco RS, Struckhoff EC, Lundquist EA. The Rac GTP exchange factor TIAM-1
724 acts with CDC-42 and the guidance receptor UNC-40/DCC in neuronal protrusion
725 and axon guidance. PLoS Genetics. Public Library of Science; 2012;8: e1002665.
726 doi:10.1371/journal.pgen.1002665

727 19. Krause M, Leslie JD, Stewart M, Lafuente EM, Valderrama F, Jagannathan R, et al.
728 Lamellipodin, an Ena/VASP ligand, is implicated in the regulation of lamellipodial
729 dynamics. Developmental Cell. 2004;7: 571–583. doi:10.1016/j.devcel.2004.07.024

730 20. Chang C, Adler CE, Krause M, Clark SG, Gertler FB, Tessier-Lavigne M, et al.
731 MIG-10/lamellipodin and AGE-1/PI3K promote axon guidance and outgrowth in
732 response to slit and netrin. Curr Biol. 2006;16: 854–862.
733 doi:10.1016/j.cub.2006.03.083

734 21. Demarco RS, Lundquist EA. RACK-1 Acts with Rac GTPase Signaling and UNC-
735 115/

736 abLIM in Caenorhabditiselegans Axon Pathfinding and

737 Cell Migration. PLoS Genetics. 2010;6: 1–17. doi:doi:10.1371/journal.pgen.100121

738 22. Shakir MA, Jiang K, Struckhoff EC, Demarco RS, Patel FB, Soto MC, et al. The
739 Arp2/3 activators WAVE and WASP have distinct genetic interactions with Rac
740 GTPases in Caenorhabditis elegans axon guidance. Genetics. 2008;179: 1957–1971.
741 doi:10.1534/genetics.108.088963

742 23. Levy-Strumpf N, Culotti JG. VAB-8, UNC-73 and MIG-2 regulate axon polarity
743 and cell migration functions of UNC-40 in C. elegans. Nature Publishing Group.
744 2007;10: 161–168. doi:10.1038/nn1835

745 24. Tang LT, Díaz-Balzac CA, Rahman M, Ramirez-Suarez NJ, Salzberg Y, Lazaro-
746 Pena MI, et al. TIAM-1/GEF can shape somatosensory dendrites independently of
747 its GEF activity by regulating F-actin localization. eLife. 2019;8: 507.
748 doi:10.7554/eLife.38949

749 25. Zou W, Dong X, Broederdorf TR, Shen A, Kramer DA, Shi R, et al. A Dendritic
750 Guidance Receptor Complex Brings Together Distinct Actin Regulators to Drive
751 Efficient F-Actin Assembly and Branching. Developmental Cell. 2018;45: 362–
752 375.e3. doi:10.1016/j.devcel.2018.04.008

753 26. Oren-Suissa M, Hall DH, Treinin M, Shemer G, Podbilewicz B. The fusogen EFF-1
754 controls sculpting of mechanosensory dendrites. Science. 2010;328: 1285–1288.
755 doi:10.1126/science.1189095

756 27. Norris AD, Sundararajan L, Morgan DE, Roberts ZJ, Lundquist EA. The UNC-
757 6/Netrin receptors UNC-40/DCC and UNC-5 inhibit growth cone filopodial
758 protrusion via UNC-73/Trio, Rac-like GTPases and UNC-33/CRMP. Development.
759 2014;141: 4395–4405. doi:10.1242/dev.110437

760 28. Maniar TA, Kaplan M, Wang GJ, Shen K, Wei L, Shaw JE, et al. UNC-33 (CRMP)
761 and ankyrin organize microtubules and localize kinesin to polarize axon-dendrite
762 sorting. Nat Neurosci. Nature Publishing Group; 2011;15: 48–56.
763 doi:10.1038/nn.2970

764 29. Chang C, Yu TW, Bargmann CI, Tessier-Lavigne M. Inhibition of netrin-mediated
765 axon attraction by a receptor protein tyrosine phosphatase. Science. American
766 Association for the Advancement of Science; 2004;305: 103–106.
767 doi:10.1126/science.1096983

768 30. Gitai Z, Yu TW, Lundquist EA, Tessier-Lavigne M, Bargmann CI. The netrin
769 receptor UNC-40/DCC stimulates axon attraction and outgrowth through enabled
770 and, in parallel, Rac and UNC-115/AbLIM. Neuron. 2003;37: 53–65.

771 31. Withee J, Galligan B, Hawkins N, Garriga G. Caenorhabditis elegans WASP and
772 Ena/VASP proteins play compensatory roles in morphogenesis and neuronal cell
773 migration. Genetics. 2004;167: 1165–1176. doi:10.1534/genetics.103.025676

774 32. Fleming T, Chien S-C, Vanderzalm PJ, Dell M, Gavin MK, Forrester WC, et al. The
775 role of C. elegans Ena/VASP homolog UNC-34 in neuronal polarity and motility.
776 Developmental Biology. 2010;344: 94–106. doi:10.1016/j.ydbio.2010.04.025

777 33. Chen C-H, Hsu H-W, Chang Y-H, Pan C-L. Adhesive L1CAM-Robo Signaling
778 Aligns Growth Cone F-Actin Dynamics to Promote Axon-Dendrite Fasciculation in

C. elegans. Developmental Cell. 2019;48: 215–228.e5. doi:10.1016/j.devcel.2018.10.028

34. Ramirez-Suarez NJ, Belalcazar HM, Salazar CJ, Beyaz B, Raja B, Nguyen KCQ, et al. Axon-Dependent Patterning and Maintenance of Somatosensory Dendritic Arbors. Developmental Cell. 2019;48: 229–244.e4. doi:10.1016/j.devcel.2018.12.015

35. Applewhite DA, Barzik M, Kojima S-I, Svitkina TM, Gertler FB, Borisy GG. Ena/VASP proteins have an anti-capping independent function in filopodia formation. Molecular Biology of the Cell. 2007;18: 2579–2591. doi:10.1091/mbc.E06-11-0990

36. Gates J, Mahaffey JP, Rogers SL, Emerson M, Rogers EM, Sottile SL, et al. Enabled plays key roles in embryonic epithelial morphogenesis in Drosophila. Development. 2007;134: 2027–2039. doi:10.1242/dev.02849

37. Liao C-P, Li H, Lee H-H, Chien C-T, Pan C-L. Cell-Autonomous Regulation of Dendrite Self-Avoidance by the Wnt Secretory Factor MIG-14/Wntless. Neuron. 2018;98: 320–334.e6. doi:10.1016/j.neuron.2018.03.031

38. Zhang W, Wu Y, Du L, Tang DD, Gunst SJ. Activation of the Arp2/3 complex by N-WASp is required for actin polymerization and contraction in smooth muscle. Am J Physiol, Cell Physiol. 2005;288: C1145–60. doi:10.1152/ajpcell.00387.2004

39. Riedl J, Crevenna AH, Kessenbrock K, Yu JH, Neukirchen D, Bista M, et al. Lifeact: a versatile marker to visualize F-actin. Nat Meth. 2008;5: 605–607. doi:10.1038/nmeth.1220

40. Smith CJ. Morphological and molecular characterization of somatosensory neurogenesis [Internet]. 2012. pp. 1–279. Available: http://login.proxy.library.vanderbilt.edu/login?url=http://search.proquest.com/docview/1627158315?accountid=14816

41. Piekny AJ, Mains PE. Rho-binding kinase (LET-502) and myosin phosphatase (MEL-11) regulate cytokinesis in the early Caenorhabditis elegans embryo. J Cell Sci. 2002;115: 2271–2282.

42. Vicente-Manzanares M, Ma X, Adelstein RS, Horwitz AR. Non-muscle myosin II takes centre stage in cell adhesion and migration. Nat Rev Mol Cell Biol. 2009;10: 778–790. doi:10.1038/nrm2786

43. Somlyo AP, Somlyo AV. Signal transduction and regulation in smooth muscle. Nature. 1994;372: 231–236. doi:10.1038/372231a0

44. Ono K, Ono S. Two distinct myosin II populations coordinate ovulatory contraction of the myoepithelial sheath in the Caenorhabditis elegans somatic gonad. Molecular

815 Biology of the Cell. American Society for Cell Biology; 2016;27: 1131–1142.
816 doi:10.1091/mbc.E15-09-0648

817 45. Schroeder NE, Androwski RJ, Rashid A, Lee H, Lee J, Barr MM. Dauer-Specific
818 Dendrite Arborization in C. elegans Is Regulated by KPC-1/Furin. Current Biology.
819 Elsevier Ltd; 2013;23: 1527–1535. doi:10.1016/j.cub.2013.06.058

820 46. Salzberg Y, Ramirez-Suarez NJ, Bülow HE. The Proprotein Convertase KPC-
821 1/Furin Controls Branching and Self-avoidance of Sensory Dendrites in
822 Caenorhabditis elegans. Chisholm AD, editor. PLoS Genetics. 2014;10: e1004657–
823 13. doi:10.1371/journal.pgen.1004657

824 47. Dong X, Chiu H, Park YJ, Zou W, Zou Y, Özkan E, et al. Precise regulation of the
825 guidance receptor DMA-1 by KPC-1/Furin instructs dendritic branching decisions.
826 eLife. eLife Sciences Publications Limited; 2016;5: 308. doi:10.7554/eLife.11008

827 48. Liu OW, Shen K. The transmembrane LRR protein DMA-1 promotes dendrite
828 branching and growth in C. elegans. Nat Neurosci. 2011. doi:10.1038/nn.2978

829 49. Sun LO, Jiang Z, Rivlin-Etzion M, Hand R, Brady CM, Matsuoka RL, et al. On and
830 off retinal circuit assembly by divergent molecular mechanisms. Science. 2013;342:
831 1241974–1241974. doi:10.1126/science.1241974

832 50. Pollitt AY, Insall RH. WASP and SCAR/WAVE proteins: the drivers of actin
833 assembly. J Cell Sci. The Company of Biologists Ltd; 2009;122: 2575–2578.
834 doi:10.1242/jcs.023879

835 51. Castellano F, Le Clainche C, Patin D, Carlier MF, Chavrier P. A WASp-VASP
836 complex regulates actin polymerization at the plasma membrane. EMBO J. 2001;20:
837 5603–5614. doi:10.1093/emboj/20.20.5603

838 52. Chen XJ, Squarr AJ, Stephan R, Chen B, Higgins TE, Barry DJ, et al. Ena/VASP
839 proteins cooperate with the WAVE complex to regulate the actin cytoskeleton.
840 Developmental Cell. 2014;30: 569–584. doi:10.1016/j.devcel.2014.08.001

841 53. Havrylenko S, Noguera P, Abou-Ghali M, Manzi J, Faqir F, Lamora A, et al.
842 WAVE binds Ena/VASP for enhanced Arp2/3 complex-based actin assembly.
843 Molecular Biology of the Cell. American Society for Cell Biology; 2015;26: 55–65.
844 doi:10.1091/mbc.E14-07-1200

845 54. Colavita A, Culotti JG. Suppressors of ectopic UNC-5 growth cone steering identify
846 eight genes involved in axon guidance in Caenorhabditis elegans. Developmental
847 Biology. 1998;194: 72–85. doi:10.1006/dbio.1997.8790

848 55. Bashaw GJ, Kidd T, Murray D, Pawson T, Goodman CS. Repulsive axon guidance:
849 Abelson and Enabled play opposing roles downstream of the roundabout receptor.
850 Cell. 2000;101: 703–715.

851 56. McConnell RE, Edward van Veen J, Vidaki M, Kwiatkowski AV, Meyer AS,
852 Gertler FB. A requirement for filopodia extension toward Slit during Robo-mediated
853 axon repulsion. The Journal of Cell Biology. 2016;213: 261–274.
854 doi:10.1083/jcb.201509062

855 57. Hung R-J, Terman JR. Extracellular inhibitors, repellents, and
856 semaphorin/plexin/MICAL-mediated actin filament disassembly. Cytoskeleton
857 (Hoboken). John Wiley & Sons, Inc; 2011;68: 415–433. doi:10.1002/cm.20527

858 58. Lin C, Espreafico E, Mooseker M, Forscher P. Myosin drives retrograde F-actin
859 flow in neuronal growth cones. Neuron. 1996;16: 769–782.

860 59. Mitchison TJ, Cramer LP. Actin-based cell motility and cell locomotion. Cell.
861 1996;84: 371–379.

862 60. Medeiros NA, Burnette DT, Forscher P. Myosin II functions in actin-bundle
863 turnover in neuronal growth cones. Nat Cell Biol. 2006;8: 215–226.
864 doi:10.1038/ncb1367

865 61. Murray A, Naeem A, Barnes SH, Drescher U, Guthrie S. Slit and Netrin-1 guide
866 cranial motor axon pathfinding via Rho-kinase, myosin light chain kinase and
867 myosin II. Neural Dev. 2010;5: 16. doi:10.1186/1749-8104-5-16

868 62. Brown JA, Wysolmerski RB, Bridgman PC. Dorsal root ganglion neurons react to
869 semaphorin 3A application through a biphasic response that requires multiple
870 myosin II isoforms. Molecular Biology of the Cell. 2009;20: 1167–1179.
871 doi:10.1091/mbc.E08-01-0065

872 63. Brown JA, Bridgman PC. Disruption of the cytoskeleton during Semaphorin 3A
873 induced growth cone collapse correlates with differences in actin organization and
874 associated binding proteins. Devel Neurobio. 2009;69: 633–646.
875 doi:10.1002/dneu.20732

876 64. Gallo G. RhoA-kinase coordinates F-actin organization and myosin II activity
877 during semaphorin-3A-induced axon retraction. J Cell Sci. 2006;119: 3413–3423.
878 doi:10.1242/jcs.03084

879 65. Fenix AM, Taneja N, Buttler CA, Lewis J, Van Engelenburg SB, Ohi R, et al.
880 Expansion and concatenation of non-muscle myosin IIA filaments drive cellular
881 contractile system formation during interphase and mitosis. Molecular Biology of
882 the Cell. 2016;27: 1465–1478. doi:10.1091/mbc.E15-10-0725

883 66. Shutova MS, Spessott WA, Giraudo CG, Svitkina T. Endogenous species of
884 mammalian nonmuscle myosin IIA and IIB include activated monomers and
885 heteropolymers. Curr Biol. 2014;24: 1958–1968. doi:10.1016/j.cub.2014.07.070

886 67. Shutova M, Yang C, Vasiliev JM, Svitkina T. Functions of nonmuscle myosin II in
887 assembly of the cellular contractile system. Parsons M, editor. PLoS ONE. Public
888 Library of Science; 2012;7: e40814. doi:10.1371/journal.pone.0040814

889 68. Matthews BJ, Grueber WB. Dscam1-mediated self-avoidance counters netrin-
890 dependent targeting of dendrites in Drosophila. Curr Biol. 2011;21: 1480–1487.
891 doi:10.1016/j.cub.2011.07.040

892 69. Nithianandam V, Chien C-T. Actin blobs prefigure dendrite branching sites. The
893 Journal of Cell Biology. 2018;217: 3731–3746. doi:10.1083/jcb.201711136

894 70. Díaz-Balzac CA, Rahman M, Lazaro-Pena MI, Martin Hernandez LA, Salzberg Y,
895 Aguirre-Chen C, et al. Muscle- and Skin-Derived Cues Jointly Orchestrate
896 Patterning of Somatosensory Dendrites. Curr Biol. 2016;26: 2379–2387.
897 doi:10.1016/j.cub.2016.07.008

898 71. Dong X, Liu OW, Howell AS, Shen K. An Extracellular Adhesion Molecule
899 Complex Patterns Dendritic Branching and Morphogenesis. Cell. 2013;155: 296–
900 307. doi:10.1016/j.cell.2013.08.059

901 72. Salzberg Y, Díaz-Balzac CA, Ramirez-Suarez NJ, Attreed M, Tecle E, Desbois M,
902 et al. Skin-Derived Cues Control Arborization of Sensory Dendritesin
903 Caenorhabditis elegans. Cell. Elsevier Inc; 2013;155: 308–320.
904 doi:10.1016/j.cell.2013.08.058

905 73. Zou W, Shen A, Dong X, Tugizova M, Xiang YK, Shen K. A multi-protein
906 receptor-ligand complex underlies combinatorial dendrite guidance choices in C.
907 elegans. eLife. eLife Sciences Publications Limited; 2016;5: e18345.
908 doi:10.7554/eLife.18345

909 74. Luo L, Wen Q, Ren J, Hendricks M, Gershow M, Qin Y, et al. Dynamic encoding of
910 perception, memory, and movement in a C. elegans chemotaxis circuit. Neuron.
911 2014;82: 1115–1128. doi:10.1016/j.neuron.2014.05.010

912

913 **FIGURE LEGENDS**

914

915 **Figure 1: Constitutively active UNC-5 retards outgrowth of 3° PVD dendrites.**

916 (A-D) Representative images and tracings of 3° dendrites anterior to PVD cell body in (A) wild
917 type (red) and (B) PVD::MYR::UNC-5 (blue) (Late L3-early L4 animals) (C) Gaussian fit to
918 distribution of lengths of PVD::mCherry-labeled 3° dendrites showing shorter average length for
919 MYR::UNC-5 (n = 156, 7 animals) *versus* wild type (n = 159, 8 animals), p = 0.03, Kolmogorov-
920 Smirnov statistical test. (D) Schematics of intact, wild-type UNC-5 receptor vs membrane-
921 associated, constitutively-activated myristylated-UNC-5 (MYR::MYR-5). (E-F) Dynamicity of 3°
922 dendrites in wild-type vs MYR::UNC-5-expressing PVD neurons labeled with PVD::GFP. (E)
923 Schematic (top) depicts displacement of the tip of a 3° dendrite relative to a fiduciary mark (vertical
924 dashed red line). Scale bar is 10 μm. Representative plots of displacement for wild-type (red) and
925 MYR::UNC-5 (blue) 3° dendrites over time. (F) The dynamic saltatory growth and retraction of
926 3° dendrites in the wild type vs the relative quiescence of MYR::UNC-5-expressing PVD neurons
927 is correlated with elevated standard deviation of tip movement from a fiduciary point in wild-type
928 vs MYR::UNC-5 expressing PVD neurons (p = 0.04 from Student's t-test. n = 4).

929

930 **Figure 2: Constitutively active UNC-5 rescues self-avoidance in an *unc-6* mutant.**

931 (A-C) Representative images (top) and tracings (bottom) of PVD dendritic architecture in late L4
932 stage larvae that are (A) PVD::MYR:UNC-5, (B) PVD::MYR::UNC-5; *unc-6(ev400),* (C) Self-
933 avoidance defects (percentage of overlapping 3° branches) are rare (< 5%) in wild type and
934 PVD::MYR::UNC-5. The Unc-6 self-avoidance defect is prevented by PVD expression of

935 MYR::UNC-5. Error bars denote mean and M. ***p<0.0001. n ≥ 15. from ANOVA with Tukey's
936 posthoc test. Scored in a PVD::mCherry background.
937
938 **Figure 3. Mutations in genes that promote actin polymerization disrupt PVD dendrite self-**
939 **avoidance.**
940 (A) Representative images (top) and schematics (bottom) of the actin cytoskeleton (green) labeled
941 with PVD::ACT-1::GFP (A) and microtubules (magenta) marked with *pdes-2*::TBA-1::mCherry.
942 PVD cell bodies (asterisks) and axons (arrowheads) are noted. (B) Representative images of
943 PVD::GFP for wild type, for *unc-34*, *mig-10*, *unc-73*, *wsp-1* mutants and for *arx-5RNAi*. Asterisks
944 denote PVD cell bodies and arrowheads point to overlaps between adjacent PVD 3° dendrites. (C-
945 E) Self-avoidance defects are plotted in a PVD::GFP background (mean and SEM) as the
946 percentage of overlapping 3° dendrites for each genotype. ***p<0.001, *p<0.05, ANOVA with
947 Tukey's posthoc test, n ≥ 15 animals for all backgrounds. (C) Self-avoidance defects for *unc-*
948 *73/Trio*, *mig-10/Lmpd* and *unc-34/Ena/VASP* mutants. Self-avoidance defects of *unc-*
949 *34/Ena/VASP* mutants are rescued by PVD expression of UNC-34 (PVD::mCherry::UNC-34).
950 Constitutively active UNC-5 (PVD::MYR::UNC-5) fails to rescue the self-avoidance defects of
951 an *unc-34* mutant. (D) PVD self-avoidance defects for *arx-5RNAi* compared to Empty Vector
952 RNAi controls., ***p<0.001 and self-avoidance defect of *unc-6*, *wsp-1* and *unc-6; wsp-1* mutants
953 compared to wildtype, NS = Not Significant, ANOVA with Tukey's posthoc test, n ≥ 15 animals.
954 Scale bar is 10 μm.
955
956 **Figure 4. Localization and trafficking of PVD::UNC-34::mCherry puncta in PVD.**

957 (A-B) iSIM images (see Methods) of PVD neurons (late L3 larvae) labeled with
958 PVD::LifeAct::GFP (green) and PVD::mCherry::UNC-34 (magenta). Merge shown at top right.
959 Insets depict punctate mCherry::UNC-34 in 1°, 2° and 3° PVD dendrites. (B) Note
960 mCherry::UNC-34 puncta at tips (white arrowheads) of 3° dendrites. Scale bars are 5 μm. (C)
961 Frequency (100%) at which tips of 3º dendrites show mCherry::UNC-34 puncta, ***p<0.001,
962 Fischer's exact test, N = 33 dendrite tips in 9 animals. Both iSIM and Airyscan images were used
963 in this analysis. (D-E) Kymographs of PVD::mCherry::UNC-34 in PVD 3° dendrite captured in
964 the iSIM microscope. Moving (green arrowheads) vs stationary (red arrowheads) mCherry::UNC-
965 34 puncta are denoted. The distal end of the 3° dendrite is indicated by an asterisk and a red dashed
966 arrow points toward the PVD cell soma. (F) Trafficking of mCherry::UNC-34 puncta in the PVD
967 3° dendrite (enclosed with rectangle of red dashed line) from 4E was analyzed using a spots
968 tracking algorithm (Imaris) (see Methods). The net displacement (μm) of mobile mCh::UNC-34
969 puncta (N = 8) from position at t = 0 in a 3º dendrite plotted against time with a sampling interval
970 of 2 s. Scale bar is 10 μm.
971
972 **Figure 5. The actin cytoskeleton is highly dynamic in PVD dendrites.**
973 (A) Time-lapse images of PVD::LifeAct::GFP and cytosolic PVD::mCherry labeled 2° dendrite
974 during outgrowth (late L3 larvae). (B) Fluorescent intensity was measured from regions of PVD
975 dendrites undergoing outgrowth vs no-outgrowth (see Materials and Methods). ***p<0.001, N =
976 118 measurements from 6 dendrites. (C) Representative image showing enriched LifeAct::GFP
977 signal in distal, growing PVD dendrites labeled with PVD::mCherry. (D) Rapid changes in the
978 normalized fluorescence intensity of PVD::LifeAct::GFP versus the PVD::mCherry cytoplasmic
979 marker were quantified as the standard deviation of the normalized fluorescent intensity measured

980 at the tips of growing dendrites. (See Movie S3 and Methods) ***p = 0.003, N = 22. (Unpaired t-
981 test) (E) Normalized fluorescence intensity measurements of PVD::LifeAct::GFP (green) vs
982 cytoplasmic PVD::mCherry (red) at the tip of a growing late L3 stage PVD 3°dendrite from a
983 representative time lapse movie.
984
985 **Figure 6. NMY-1/non-muscle myosin II mediates dendrite self-avoidance**.
986 (A) Representative images (left) and tracings (right) of wild type and *nmy-1(sb113)* labeled with
987 PVD::GFP. Arrowheads mark overlapping 3° dendrites. The PDE neuron (asterisk) is adjacent to
988 the PVD cell-body. (B) NMY-1 fused to GFP via a linker peptide (PVD::GFP::NMY-1) (top)
989 expressed in PVD with PVD::mCherry (bottom) rescues self-avoidance defects (C) of *nmy-*
990 *1(sb113)*. Scale bars are 5µm. (D) Quantification of self-avoidance defects in wild type and *nmy-*
991 *1*. The percentage of overlapping 3° branches is elevated in *nmy-1* mutants and with *nmy-1* cell-
992 specific RNAi (csRNAi) vs wild type. PVD expression of GFP-labeled NMY-1
993 (PVD::GFP::NMY-1) rescues the *nmy-1(sb113)* self-avoidance defect. Scatter plots with mean
994 and SEM, ***p<0.01, One way ANOVA with Tukey's posthoc test. N = 15-20 animals per
995 genotype. All defects were quantified in a PVD::GFP background. Scale bar is 5 µm.
996
997 **Figure 7. Phosphomimetic activation of myosin regulatory light chain, MLC-4, retards**
998 **outgrowth of 3° PVD dendrites.**
999 (A) Phosphorylation of Regulatory Light Chain (RLC) induces a conformational change that
1000 activates the myosin protein complex composed of myosin heavy chain (MHC), essential light
1001 chain (ELC) and RLC. (B) Threonine and serine phosphorylation sites (red) in conserved regions
1002 of *C. elegans*, *Drosophila* and human myosin RLCs. (C) Phosphomimetic construct,

1003 PVD::GFP::MLC-4-DD, fused to GFP with a linker peptide for expression with PVD promoter.
1004 (D-E) Representative images (top) and schematics (bottom) of PVD morphology anterior to cell
1005 body (asterisk) denoting 3° dendrites for (D) wild type (red) and (E) MLC-4DD (blue) (L3 stage
1006 larvae). Wild-type image also used in Figure 2A. Scale bars are 10 μm. 3° dendrite length (F) is
1007 shorter and gaps between 3° dendrites (G) is wider for MLC-4DD versus wild type at the L3 stage.
1008 Gaussian fit was plotted with bin center values (μm) on the X-axis and the number of values that
1009 fall under each bin center on the Y axis, ***$p<0.001$, Kolmogorov-Smirnov test for cumulative
1010 distributions of PVD 3° dendrite lengths and length of gaps in MLC-4DD (n = 141, 6 animals)
1011 versus wild type (n = 156, 8 animals). Scale bar is 10 μm.
1012
1013 **Figure 8. Phosphomimetic activation of myosin regulatory light chain, MLC-4, rescues the**
1014 ***unc-6* dendritic self-avoidance defect.**
1015 (A-B) Representative images and tracings of PVD dendritic architecture in late L4 stage larvae
1016 expressing (A) PVD::MLC-4DD or (B) PVD::MLC-4DD; *unc-6(ev400)*. (C) PVD expression of
1017 MLC-4DD rescues the *unc-6* mutant self-avoidance defect, ***$p<0.0001$, One way ANOVA with
1018 Tukey's posthoc test. Mean and SEM are shown. $n \geq 9$ animals per genotype. Quantified with
1019 PVD::mCherry. Scale bar is 10 μm. wild-type and *unc-6(ev400)* results from Figure 2D.
1020
1021 **Figure 9. Opposing pathways regulate dendrite outgrowth versus retraction.**
1022 Representative images and schematics of PVD in (A) *kpc-1/kpc-1,* (B) *kpc-1/+; unc-6/+* and (C)
1023 *kpc-1 +/+ dma-1; unc-6/+*. PVD soma (asterisks) and overlapping 3° dendrites (arrowheads) are
1024 noted. (D) Quantification of self-avoidance defects for each genotype. Note that all mutant alleles
1025 are recessive but that *kpc-1/+; unc-6/+* double heterozygotes show a strong self-avoidance defect

1026 that is suppressed in *kpc-1* +/+ *dma-1; unc-6*/+ triple heterozygotes. ***p<0.0001, one way
1027 ANOVA with Tukey's posthoc test. Mean and SEM are indicated. *** p <0.0001, N ≥7 animals
1028 per genotype. PVD is labeled with *ser2prom3*::GFP for all images. Scale bar is 10 μm. Mutant
1029 alleles were: *kpc-1(xr58), unc-6(ev400)* and *dma-1(wy686)*. (E) Model of opposing pathways that
1030 promote actin polymerization to define dendrite length. KPC-1 antagonizes surface expression of
1031 DMA-1 that interacts with an epidermal receptor composed of SAX-7/CAM, MNR-1 and LECT-
1032 2 and functions with HPO-30 to activate TIAM-1/GEF and the Wave Regulatory Complex (WRC)
1033 for actin polymerization and dendrite outgrowth. UNC-6/Netrin is captured by UNC-40/DCC for
1034 interaction with UNC-5 to activate UNC-34/Ena/VASP which functions with WSP-1/WASP and
1035 the Arp2/3 complex to drive F-actin assembly for NMY-1/myosin-dependent dendrite retraction
1036 in the self-avoidance response. (UNC-73/Trio and MIG-10/Lamellipodin are not shown to
1037 simplify the diagram, see Results). Homotypic interaction of MIG-14/Wntless in contacting 3°
1038 dendrites also drives retraction possibly through WSP-1.
1039
1040

1041 **SUPPORTING INFORMATION.**

1042

1043 **Airy Scan imaging and analysis.** Animals were immobilized with 15mM levamisole/0.05%
1044 tricaine and mounted on 10% agarose pads in M9 buffer. Z stacks were captured using a Plan Apo
1045 63x, 1.40 NA objective on a Zeiss LSM880 inverted fluorescence microscope outfitted with Airy
1046 Scan technology (Carl Zeiss Microscopy). Images of PVD::LifeAct::GFP and
1047 PVD::mCherry::UNC-34 (Figure S3 A-B) were processed to achieve Airy Scan (1.7x) super
1048 resolution and cropped using Fiji/ImageJ.

1049

1050 **TIRF microscopy and analysis.** Animals were immobilized with 15mM levamisole/ 0.05%
1051 tricane and mounted on 2% agarose pads in M9 buffer. The coverslip placed on top of the agarose
1052 pad encasing the immobilized worms is 1mm in thickness. Time-lapse datasets were acquired
1053 using a Nikon TiE inverted fluorescence microscope outfitted with a TIRF illuminator, Apo TIRF
1054 100x, 1.49NA oil immersion objective, and NIS-Elements software (Nikon Instruments, Inc.). The
1055 images for time lapse videos of PVD::mCherry::UNC-34 (Figure S3C) were captured in a single
1056 plane at 15 frames/sec and the TIRF angle was adjusted for oblique illumination of 3° PVD
1057 dendrites. Datasets were imported into FIJI/ImageJ for further analysis.

1058

1059 **Imaging and quantification of self-avoiding 3° dendrites:**

1060 **Condition 1**: (See Figure S4A-C) L3 animals of strain
1061 CLP928 *twnEx382[Pser2.3::LifeAct::EGFP, Pser2.3::mCherry, Pgcy-8::gfp]* [37] were
1062 immobilized for time-lapse imaging with 1 μl of agarose beads (Polybead carboxylate
1063 microspheres, Polysciences, Catalog # 15913-10, 0.05 μm) and mounted on a 10% agarose pad.

1064 Z-stacks of PVD dendrites (0.5 um depth, 5 slices) were imaged at both 35 second intervals with
1065 a 40X objective in a Nikon spinning disk confocal microscope. Contact between the 3° dendrites
1066 was established as a function of max feret (maximum distance between 2 points). Max feret (in
1067 pixels) was measured in the mCherry channel (cystosolic marker) with NIS elements and contact
1068 defined as the time-point at which the max-feret approaches zero. LifeAct::GFP and mCherry
1069 signals were measured for a ROI of 2 μm at the tips of the left and right dendrites in a single Z
1070 plane. Left and right fluorescence intensities were summed for comparison to a control ROI (2
1071 μm) in an adjacent non-contacting region. The change in fluorescence intensity (ΔF) for each
1072 contact and control region was calculated as the difference between the signal at contact (F_t) and
1073 the fluorescence value at two time points prior to contact (F_{t-2}) normalized to F_{t-2} or $\Delta F = (F_t - F_{t-$
1074 $_2)/F_{t-2}$ [37]. These values were computed for contact and control ROIs for LifeAct::GFP and
1075 mCherry. Statistical tests used for comparison between the datasets (LifeAct::GFP contact vs
1076 control, mCherry contact vs control, LifeAct::GFP contact vs. mCherry contact) were 2-way
1077 ANOVA with Bonferroni correction and multiple t-tests with a False Discovery Rate of 1%. Both
1078 these tests yielded similar results. No significant differences were detected in the LifeAct::GFP
1079 signal in contacting vs non-contacting regions of 3° dendrites.
1080 **Condition 2**: Late L3 larvae of P*F49H12.4::LifeAct::GFP; PF49H12.4::mCherry* were
1081 immobilized as above for imaging in the spinning disk confocal microscope. Z-stacks of PVD
1082 dendrites were imaged at either 1 or 1.30 minute intervals with a 100X objective (See Figure S4D).
1083 Contact is defined by the point at which the max feret (maximum distance between 2 points)
1084 between adjacent PVD 3º dendrites in the mCherry channel approached zero. For comparisons of
1085 LifeAct::GFP signals at the tips of 3º dendrites before and during contact, fluorescence intensities

1086 were determined from a 5 μm ROI centered at the point of contact and from a contiguous control
1087 (non-contact) 5 μm ROI positioned either to the left or right of the contact region (Figure 6F). The
1088 change in fluorescence intensity (ΔF) for each contact and control region was calculated as the
1089 difference between the signal at contact (F_t) and the fluorescence value at two time points prior to
1090 contact (F_{t-2}) normalized to F_{t-2} or $\Delta F = (F_t - F_{t-2})/F_{t-2}$ [37]. For all measurements, the cytoplasmic
1091 mCherry marker was monitored to measure the Max Feret (in this case, maximum distance
1092 between two points) between the tips of adjacent 3º dendrites and the point of contact determined
1093 when the Max Feret approaches zero. Statistical comparisons (N = 8) were performed with a 2-
1094 way ANOVA with Bonferroni correction (Figure S4D). For representative traces shown in Figure
1095 S4, Nikon NIS Elements was used to obtain LifeAct::GFP and mCherry fluorescence
1096 measurements from a 1 μm ROI at the tips of the left and right 3º dendrites undergoing contact.
1097 Fluorescence intensity measurements of LifeAct::GFP and mCherry for the opposing dendrites
1098 were normalized against the maximum value for each fluorophore and plotted vs time.
1099

1100 **Supplemental Figure 1: UNC-6/Netrin signaling mediates sister dendrite self-avoidance.**
1101 (A-B) Representative images and tracings of PVD sensory neurons in wild-type (A) and *unc-6* (B)
1102 L4-stage larvae. PVD morphology was visualized with PVD::GFP or PVD::mCherry markers.
1103 PVD cell body marked with an asterisk. (A) 1°, 2°, 3° and 4° dendritic branches and single axon
1104 (blue arrowhead) are denoted. (B) Red arrowheads point to overlaps between adjacent 3° dendrites
1105 that failed to self-avoid in *unc-6* mutants. Scale bars are 5 μm. C) Summary of self-avoidance in
1106 3° PVD dendrites denoting growth, contact and retraction. (D) Model of self-avoidance

1107 mechanism involving reciprocal contact-dependent repulsion mediated by UNC-6/Netrin and its
1108 receptors, UNC-40/DCC and UNC-5 [9].
1109
1110 **Supplemental Figure 2. Mutations in *unc-34/Ena/VASP* and *unc-73/Trio* disrupt PVD**
1111 **dendrite morphology.**
1112 Quantification of 1° dendrite outgrowth and (B) number of 2° dendrites in wild-type, *unc-34*, *unc-*
1113 *73*, *wsp-1* and PVD::mCherry::UNC-34*;unc-34*. Defective 1° dendrites show altered alignment
1114 and/or extension defects. Mutations in *unc-34* and *unc-73* but not *wsp-1* result in defective 1°
1115 dendrite outgrowth and fewer 2° dendrites. Note that expression of UNC-34::mCherry in PVD
1116 restores 3° self-avoidance (Figure 3C) but does not rescue 1° and 2° dendritic defects which
1117 suggests that UNC-34 function could be required in other cell types for normal PVD 1° and 2°
1118 outgrowth , *p=0.02, **p=0.003, ***p<0.001, Fisher's exact and 2-way ANOVA with Tukey's
1119 correction for multiple comparison. (C) Representative images of PVD morphological defects in
1120 an *unc-34* mutant. Note premature termination of 1° dendrites (red arrowheads). (D)
1121 Representative image and drawing of PVD branching defects in a *tiam-1/GEF* mutant at the L4
1122 stage. Scale bars are 10 μm. Mutant alleles are *unc-34(gm104), unc-73(rh40)*, *wsp-1 (gm324)* and
1123 *tiam-1(tm1556)*.
1124
1125 **Supplemental figure 3. Localization and trafficking of PVD:: mCherry ::UNC-34 puncta in**
1126 **PVD using Airy Scan and TIRF microscopy.**
1127 (A) Zeiss Airyscan images of PVD simultaneously labeled with PVD::LifeAct::GFP (green) and
1128 PVD::mCherry::UNC-34 (Magenta). Merge shown on right. Insets denote PVD dendrites (B).
1129 White arrows indicate 2°, 3°, and 4° dendrites. Scale bar is 10 μm. (C) Kymographs of

1130 PVD::mCherry::UNC-34 in PVD 1° dendrite captured in the Nikon TIRF microscope.
1131 Anterograde (white) and retrograde (red) movements of mCherry::UNC-34 puncta are denoted.
1132
1133 **Supplemental figure 4. Actin dynamics during dendrite self-avoidance**
1134 Schematic (left) of adjacent 3° dendrites and representative time lapse series (35 sec intervals) of
1135 PVD::mCherry and PVD::LifeAct::GFP in 3° dendrites showing self-avoidance response
1136 (Condition 1). Point of contact is indicated by an asterisk and period of contact denoted with
1137 dashed blue outline. Scale bar is 10 μm. (B) Schematic depicting ROIs for fluorescence intensity
1138 measurements at the tips of adjacent (left vs right) 3° dendrites that undergo contact and at an
1139 adjacent non-contact (control) region. (C) Graphical representation of the change in fluorescence
1140 intensity at each time point vs that of 2 time intervals (t-2) before contact (t = 0); Measurements
1141 were normalized to fluorescence intensity at t-2 or (F_{t-2}) [37] . Normalized fluorescence intensity
1142 values were plotted against time (min) for LifeAct::GFP contacting 3° dendrites vs non-contact,
1143 and were compared by 2-way Anova with Bonferonni correction, $p = 0.54$ (N=14). (D) Time lapse
1144 series collected with 100X objective at 1-1.3 minute intervals (N = 8) (Condition 2). The values
1145 for LifeAct::GFP at contact vs non-contacting region of 3° dendrites at each time-point were
1146 compared by 2-way Anova with Bonferonni correction, $p = 0.74$, NS (Not Significant).
1147
1148 **Supplemental Figure 5**: **Actin dynamics during dendrite self-avoidance**
1149 (A-D) Fluorescent intensity traces wild-type PVD dendrites during 3° dendrite self-avoidance.
1150 Fluorescent intensity measurements of PVD::LifeAct::GFP and PVD::mCherry were acquired at
1151 either 1 min (A-B) or 1.3 min (C-D) intervals from a 1μm region at the tips of the growing and
1152 contacting left and right 3° dendrites (Late L3-L4 animals). Measurements were normalized

1153 against the maximum intensity during a ~10 minute interval that includes at least one contact event.
1154 The gap between the left and right 3° dendrites undergoing contact was determined from the
1155 cytoplasmic mCherry signal and plotted against time. The period of contact (vertical shading)
1156 corresponds to a minimum value for the gap (0-0.14μm) between contacting left and right 3°
1157 dendrites. (E) Representation of 3° dendrites with color schemes to indicate left and right 3°
1158 dendrites and 1μm regions quantified.
1159
1160 **Movie S1: Time-lapse video representing the dynamic movement of 3° dendrites in a wild-**
1161 **type background.** Images of PVD::GFP were recorded (late L3-early L4) at 15 sec intervals with
1162 a 100X objective in a Nikon spinning disk microscope (see Materials and Methods). The length of
1163 the video is 240 seconds. The movie was edited using NIS elements software with Bayes advanced
1164 denoising. Green arrowheads denote the tips of 3° dendrites. Scale bar is 25 μm.
1165
1166 **Movie S2: Time-lapse video of 3° dendrites in a PVD::MYR::UNC-5.** Images of PVD::GFP
1167 in the PVD::MYR::UNC-5 strain were recorded (late L3-early L4) at 15 sec intervals with a 100X
1168 objective in a Nikon spinning disk microscope (see Materials and Methods). The entire length of
1169 the video is 12 minutes. Boxes denote tips of 3° dendrites showing limited outgrowth**.** The movie
1170 was edited using NIS elements software with Bayes advanced denoising. Scale bar is 10μm.
1171
1172 **Movie S3: Time-lapse video showing the dynamicity of LifeAct::GFP during in 3° PVD**
1173 **dendrites**. Images of PVD::mCherry (left) and PVD::LifeAct::GFP (right) and were collected at
1174 1.3 min intervals with a 100 X objective in a Nikon spinning disk microscope (see Materials and

1175 Methods). The entire length of the video is 60 minutes. The movie was edited using NIS elements
1176 with automatic deconvolution. Scale bar is 5 μm. Spherical objects are autofluorescent granules.
1177
1178 **Movie S4: Time-lapse video showing dynamic LifeAct::GFP signal in 3° sister dendrites**.
1179 Images of PVD::mCherry (left) and PVD::LifeAct::GFP (right) and were collected at 1.3 min
1180 intervals with a 100 X objective in a Nikon spinning disk microscope (see Materials and Methods).
1181 The length of the video is 60 minutes. The movie was edited using NIS elements with automatic
1182 deconvolution. Arrows track 3º dendrites undergoing contact and retraction. Scale bar is 5 μm.
1183
1184 **Movie S5: Time-Lapse video demonstrating the trafficking of UNC-34::mCherry puncta in**
1185 **PVD 3° dendrites.** Images of PVD::mCherry::UNC-34 were captured at 2 minute intervals in a
1186 single Z plane with a 100X objective in a iSIM microscope for 3 minutes (See Materials and
1187 Methods). Tips of 3° dendrites are indicated by a magenta arrowhead. The movie was edited using
1188 a Metamorph and deconvolved using Fiji software. Scale bar is 5 μm.

Figure 1: Constitutively active UNC-5 drives slows outgrowth of 3º PVD dendrites.

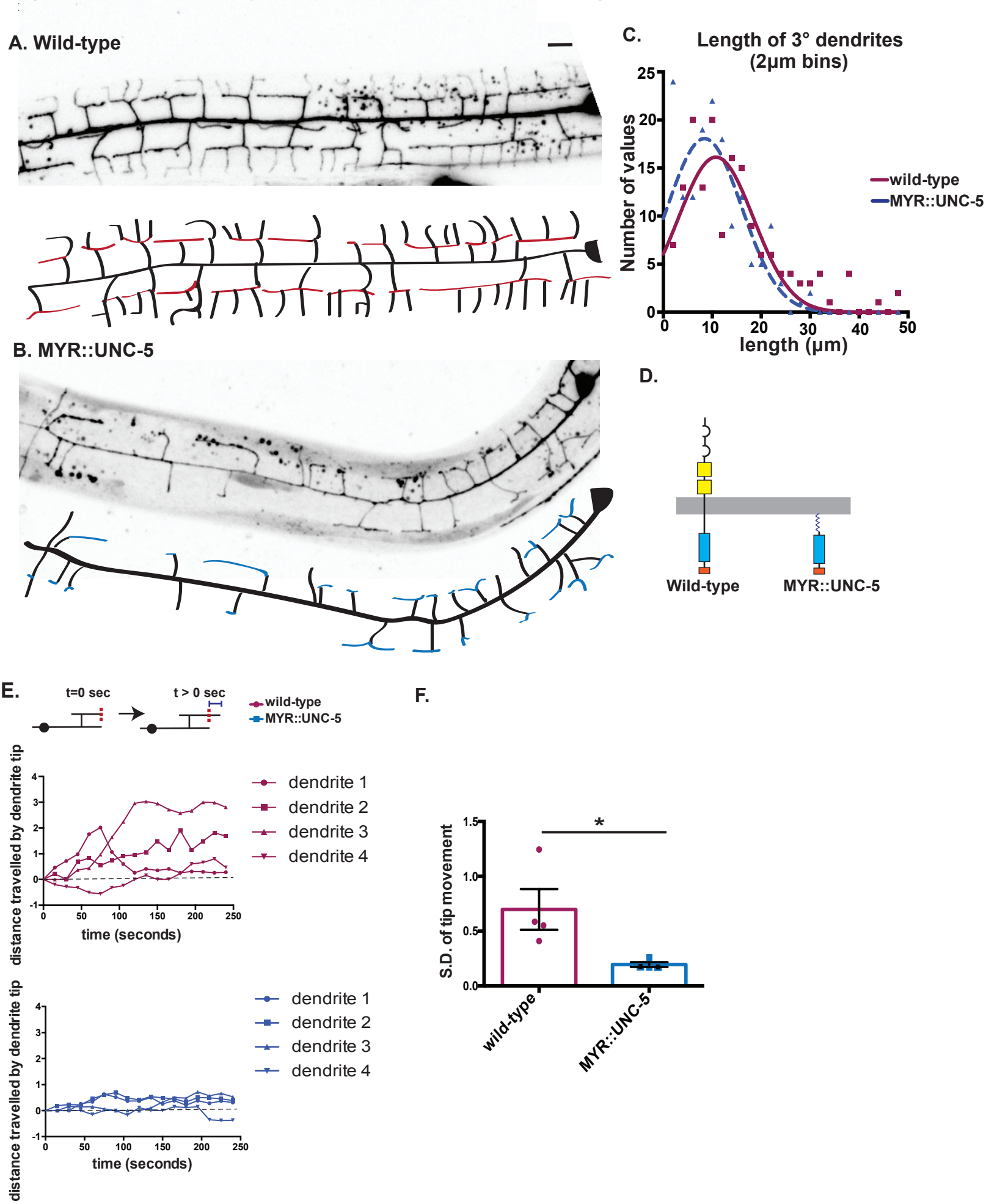

Figure 2: Constitutively active UNC-5 drives decelerated outgrowth of 3º PVD dendrites.

A.

PVD::MYR::UNC-5

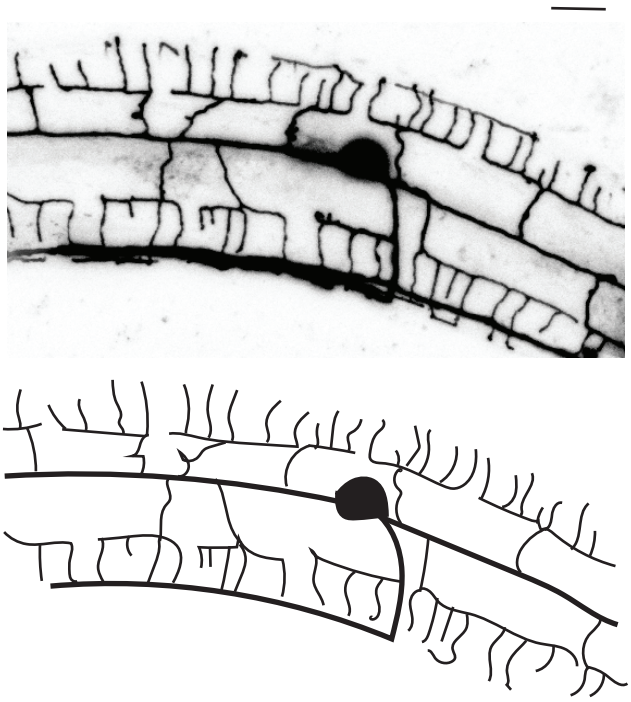

B.

PVD::MYR::UNC-5; unc-6

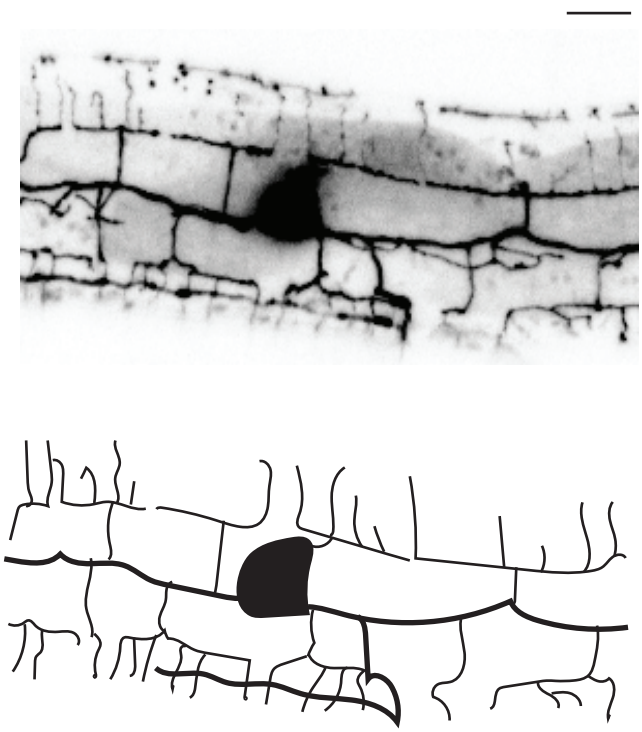

C. *tiam-1(tm1556)*

D.

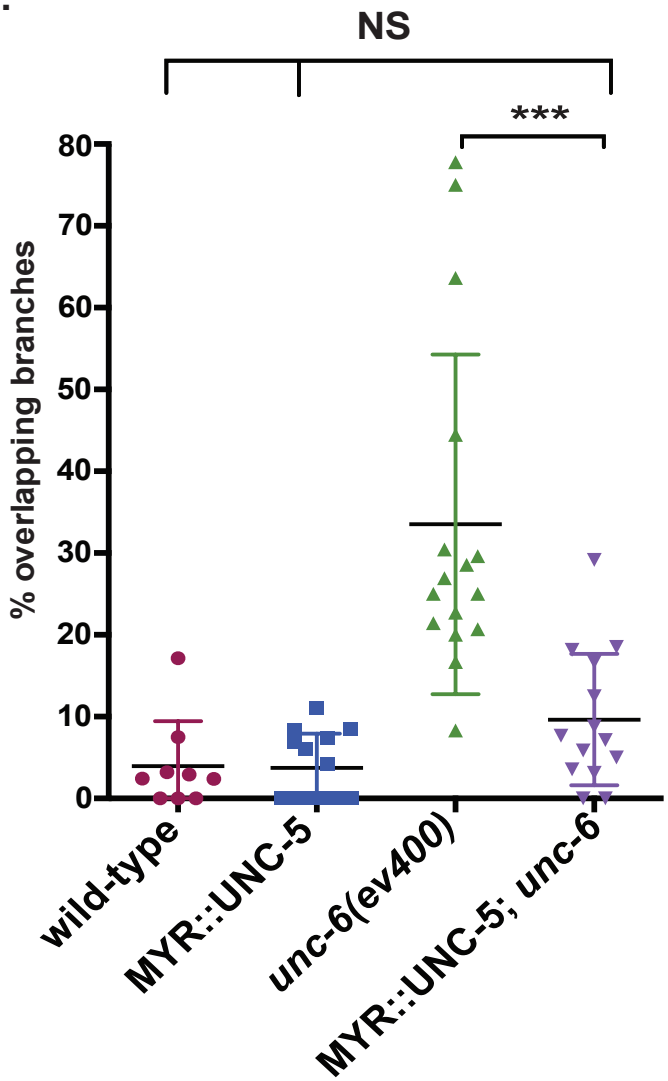

Figure 3: Mutations in genes that promote actin polymerization disrupt PVD dendrite self-avoidance.

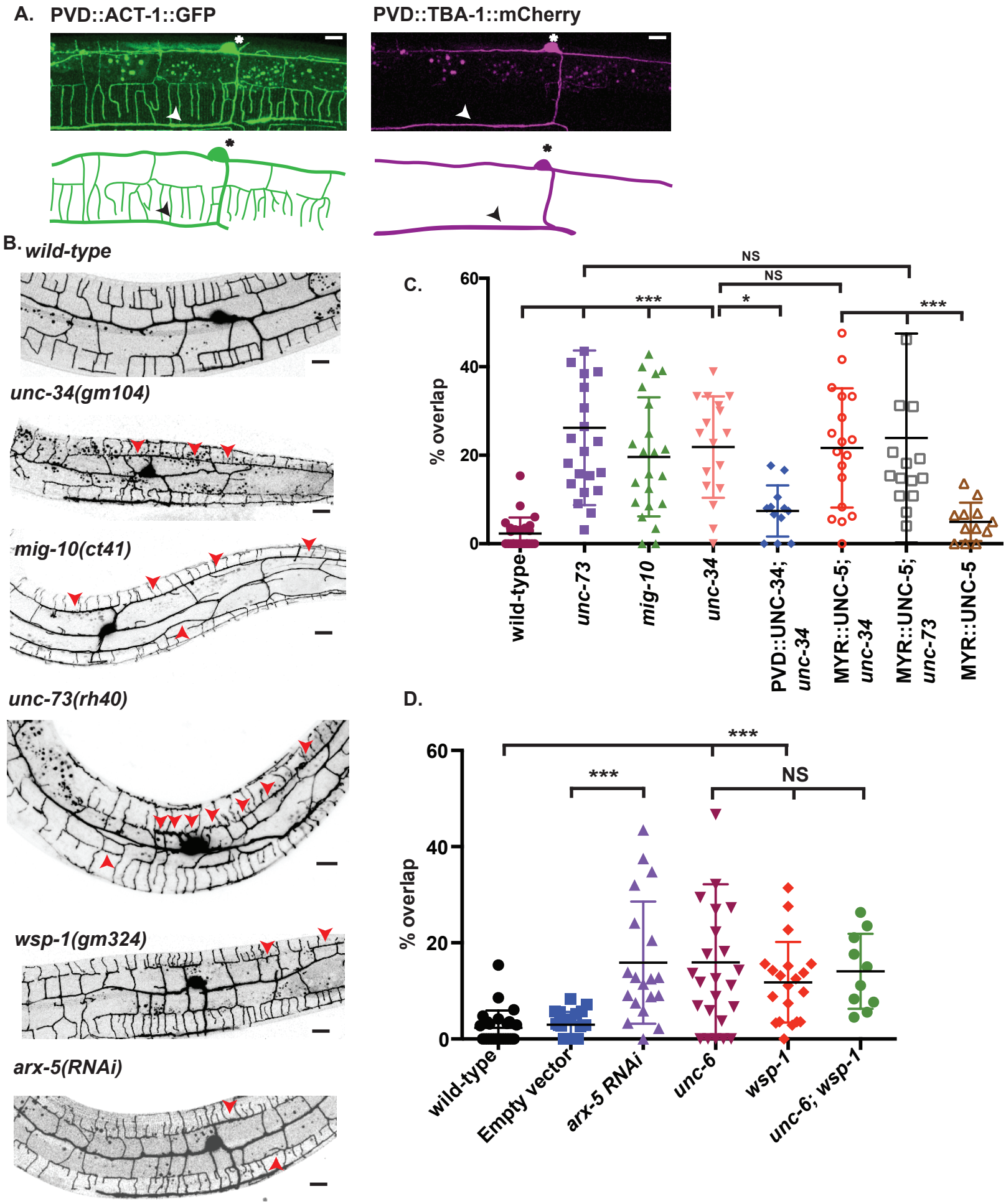

Figure 4: Localization and trafficking of PVD::UNC-34::mCherry puncta in PVD.

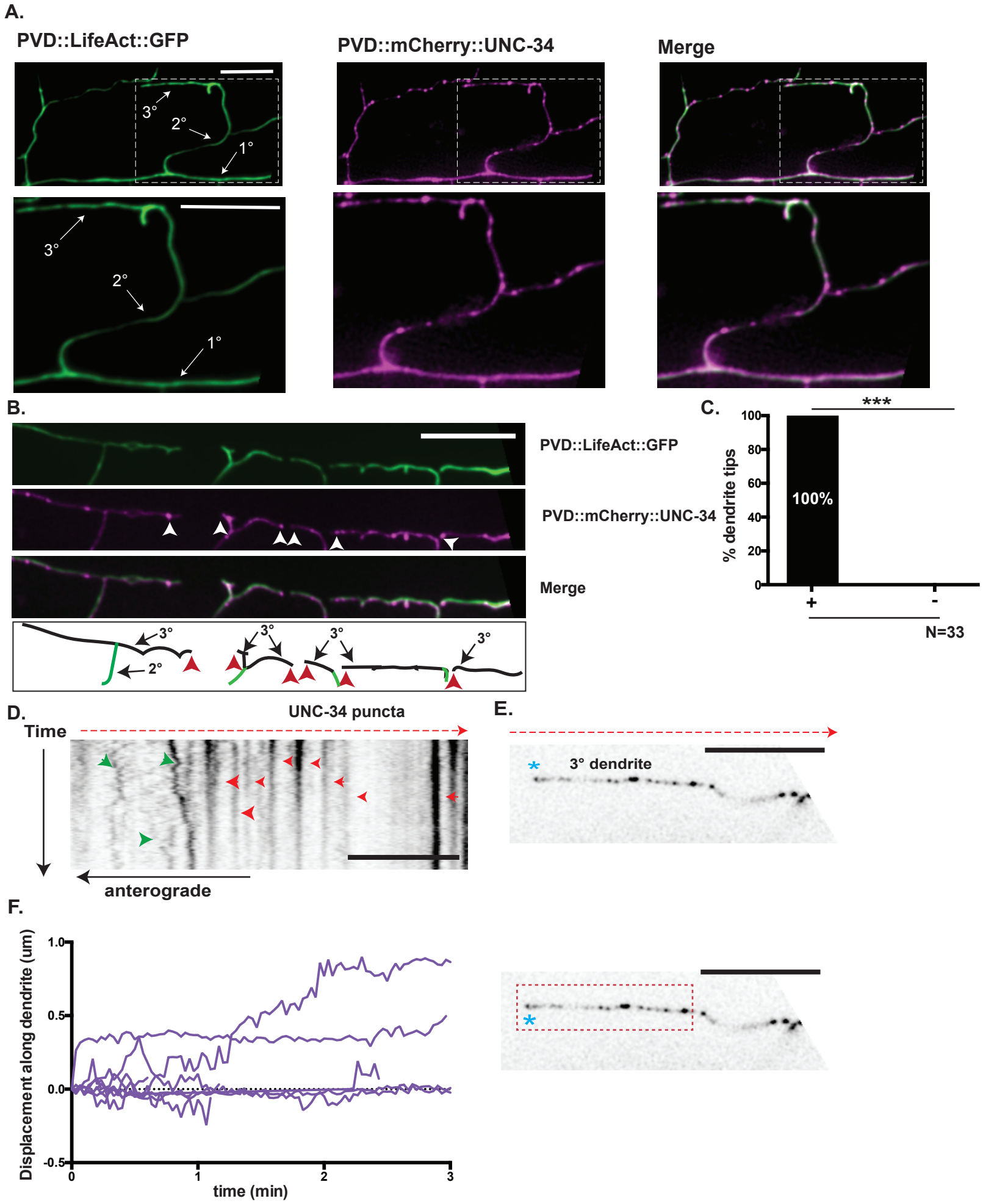

Figure 5: The actin cytoskeleton is highly dynamic in PVD dendrites

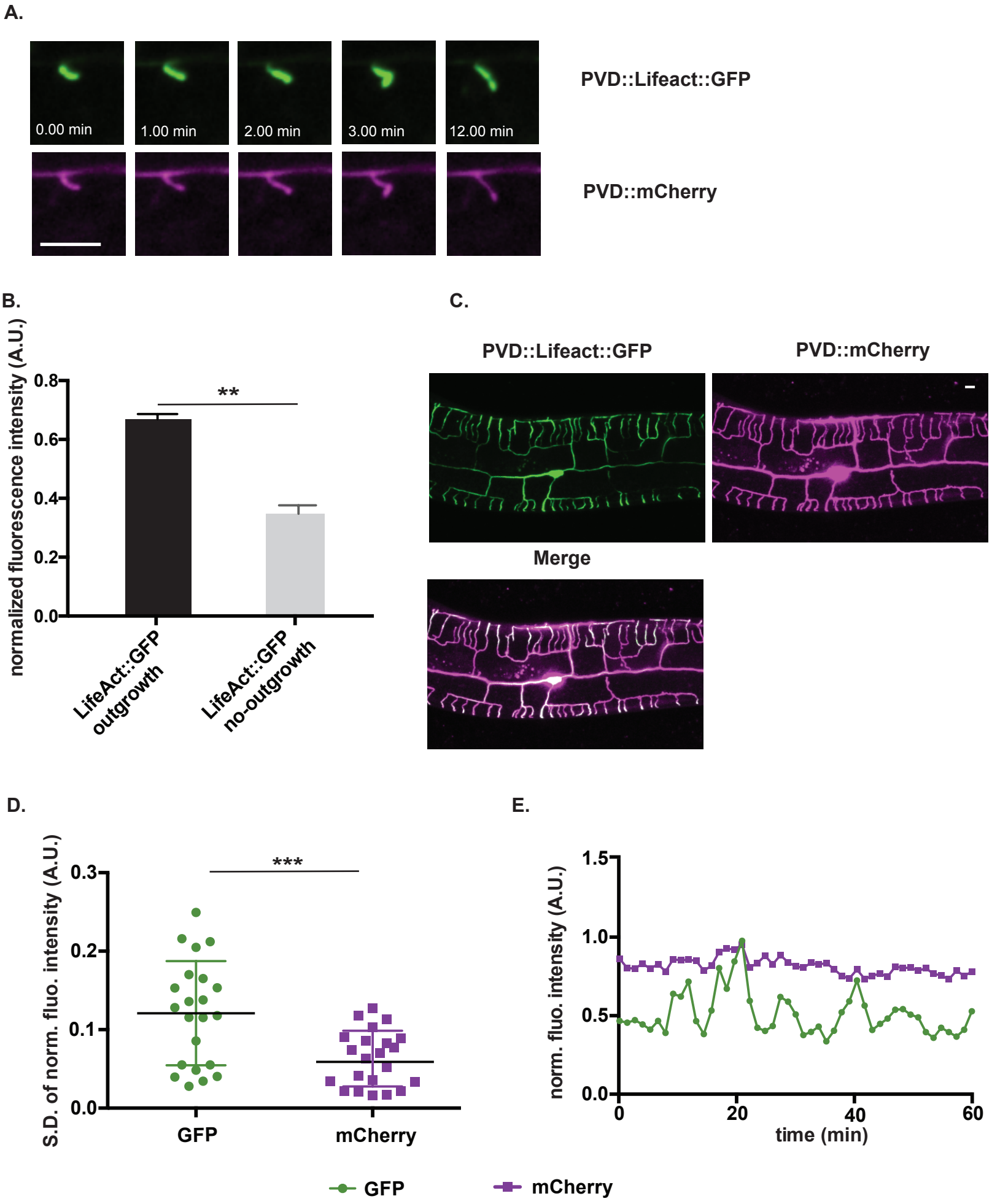

Figure 6: NMY-1/non-muscle myosin II mediates dendrite self-avoidance.

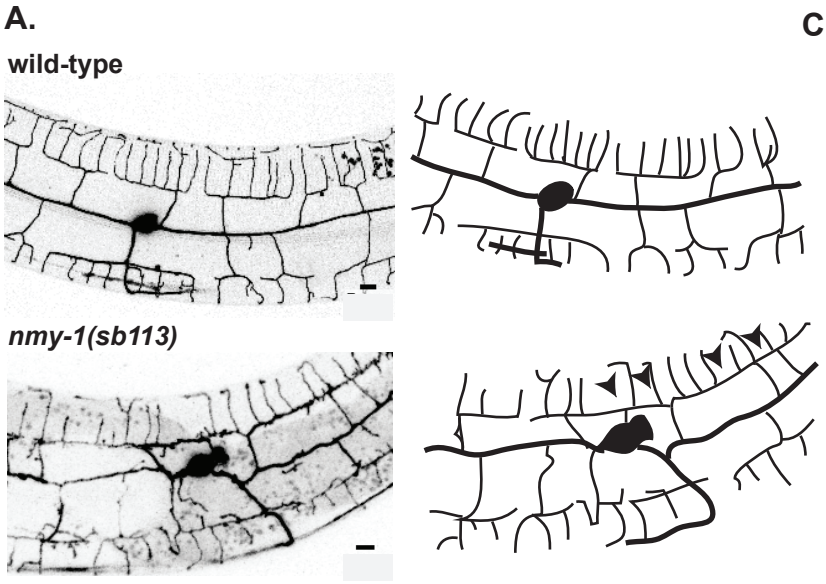

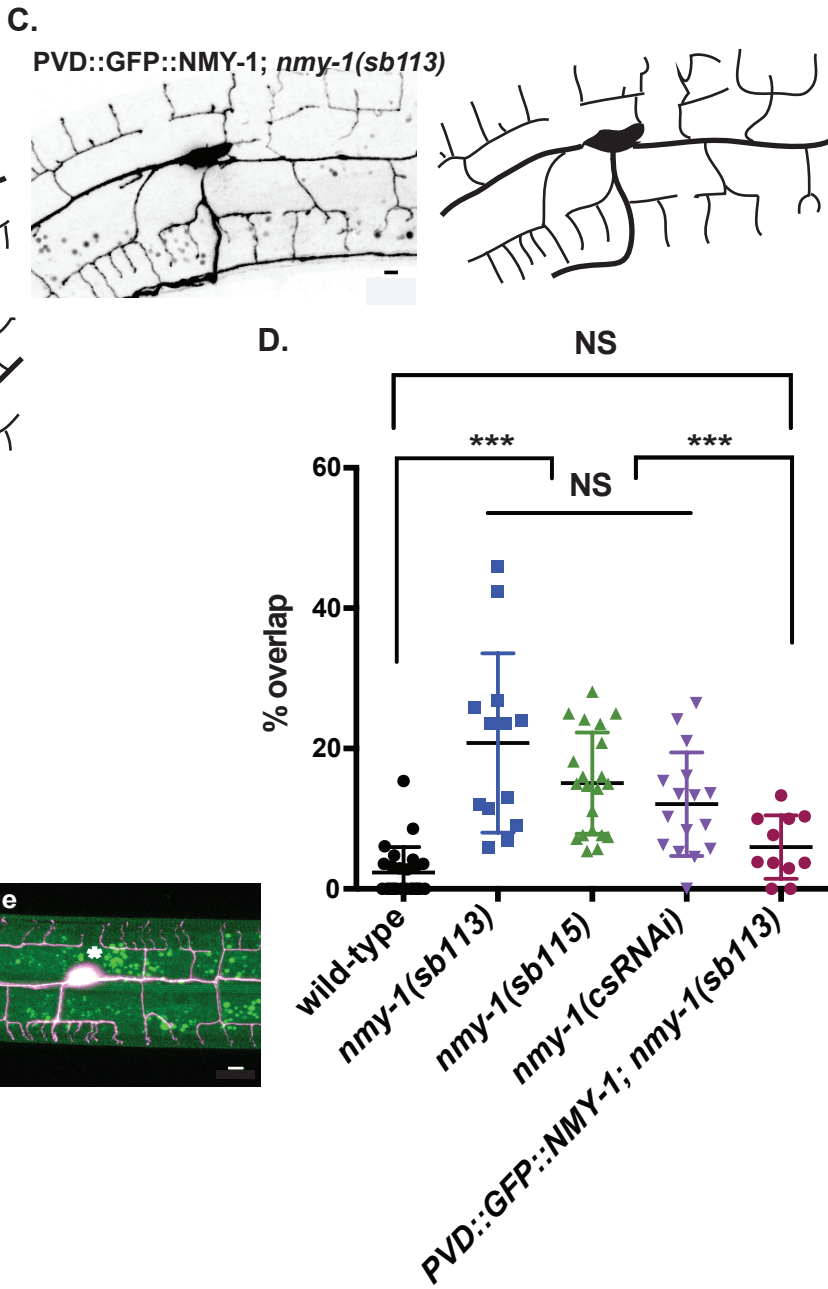

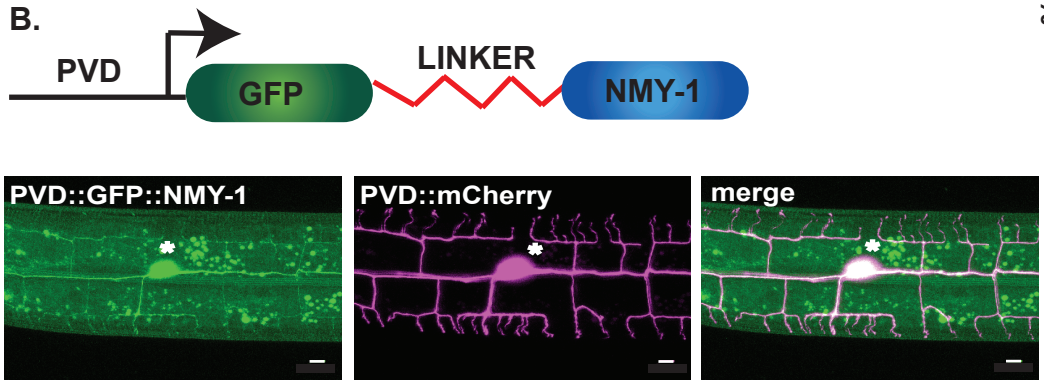

Figure 7: Phosphomimetic activation of myosin regulatory light chain, MLC-4, slows outgrowth of 3º PVD dendrites.

A.

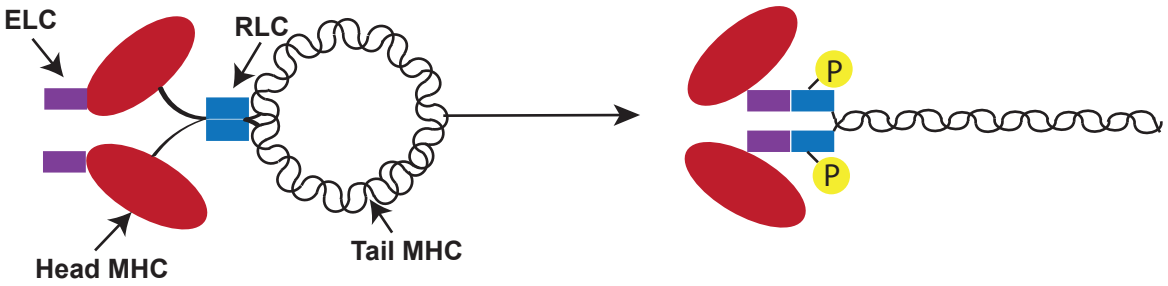

B.

C. elegans	MLC-4	QRATSNVFAMFDQ
D. melanogaster	MRLC-C	QRATSNVFAMFDQ
H. sapiens	MRLC2	QRATSNVFAMFDQ

C.

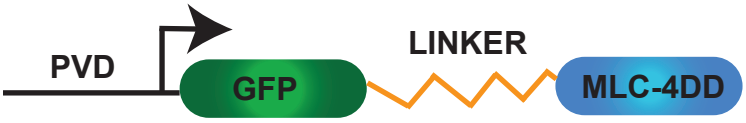

D.

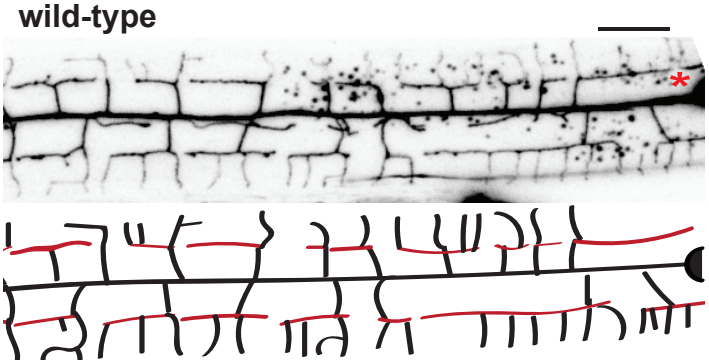

E.

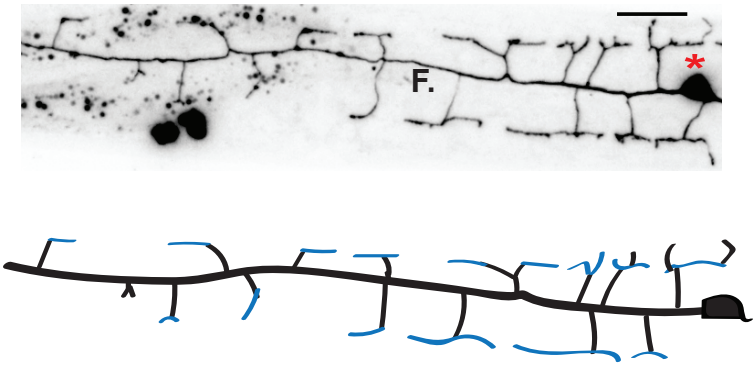

F.

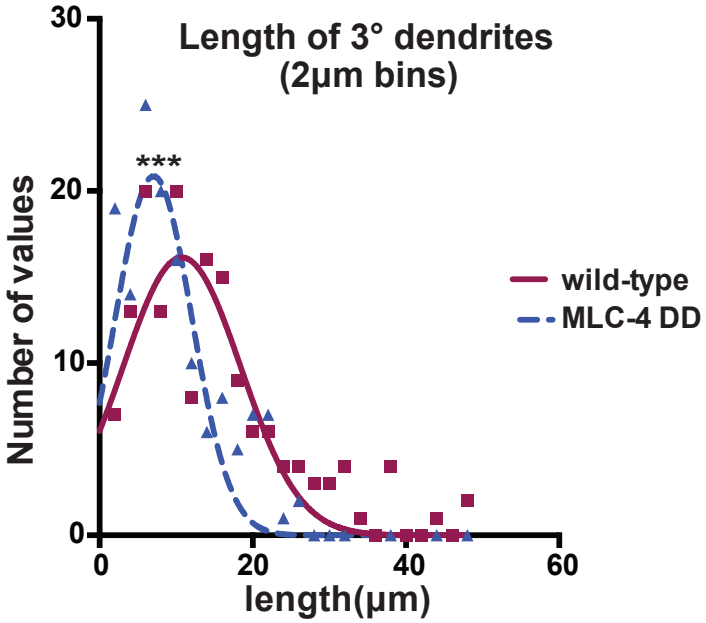

G.

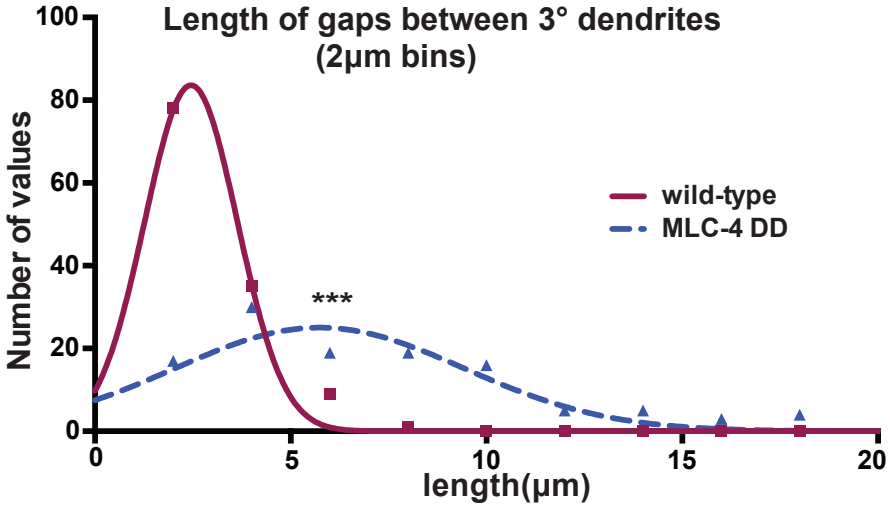

Figure 8: Phosphomimetic activation of myosin regulatory light chain, MLC-4, rescues the *unc-6* dendritic self-avoidance defect.

A.

PVD::MLC-4DD

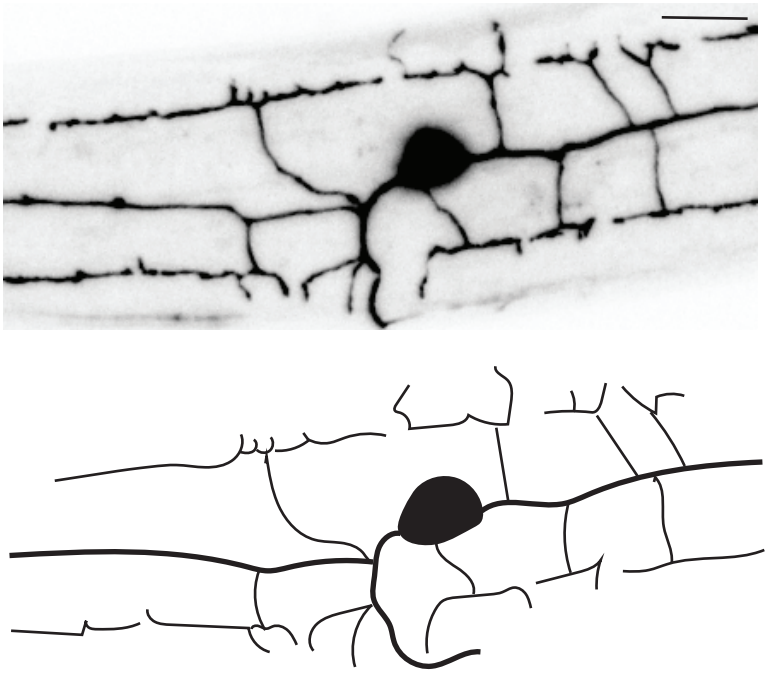

B.

PVD::MLC-4DD; unc-6

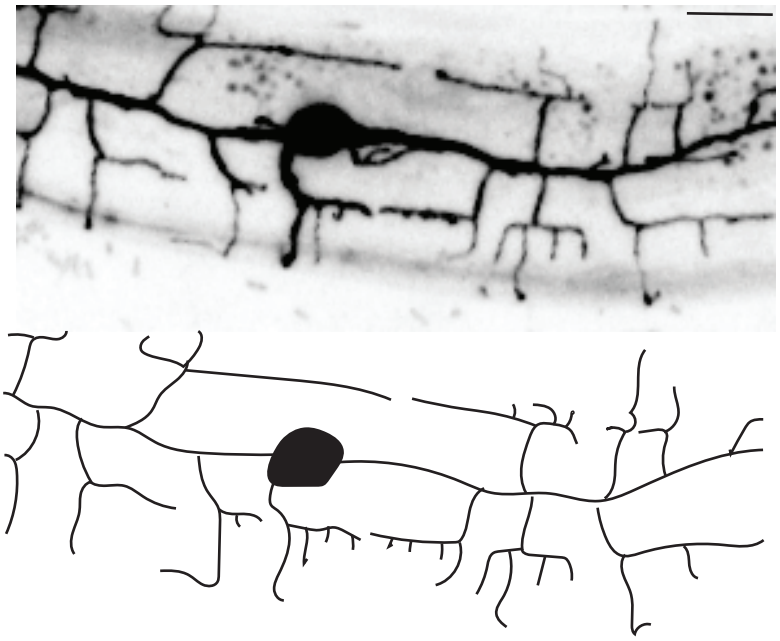

C.

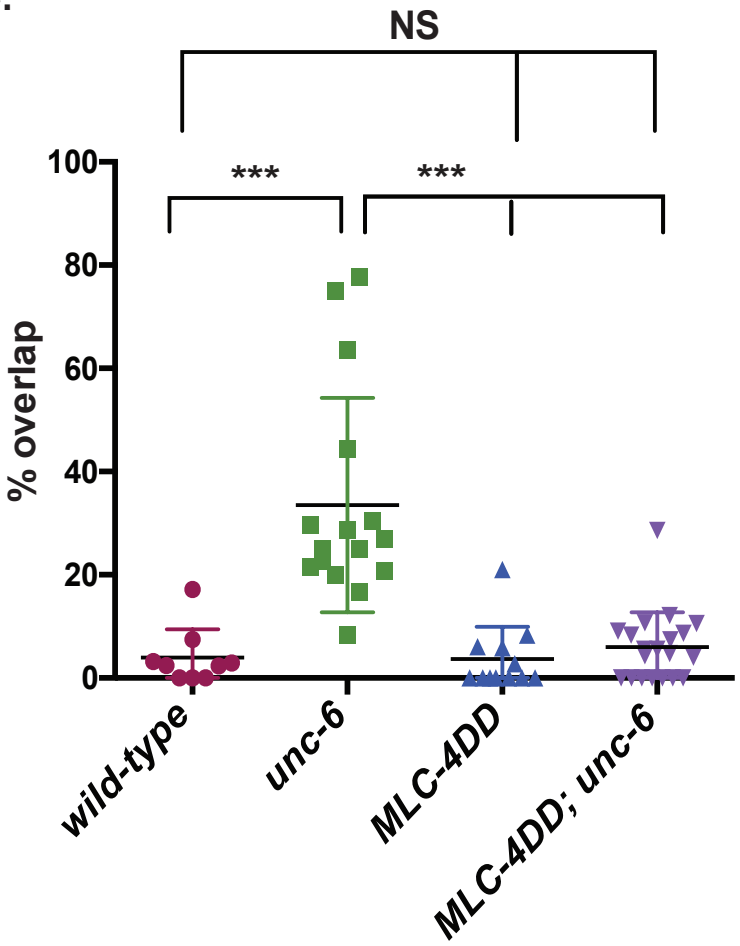
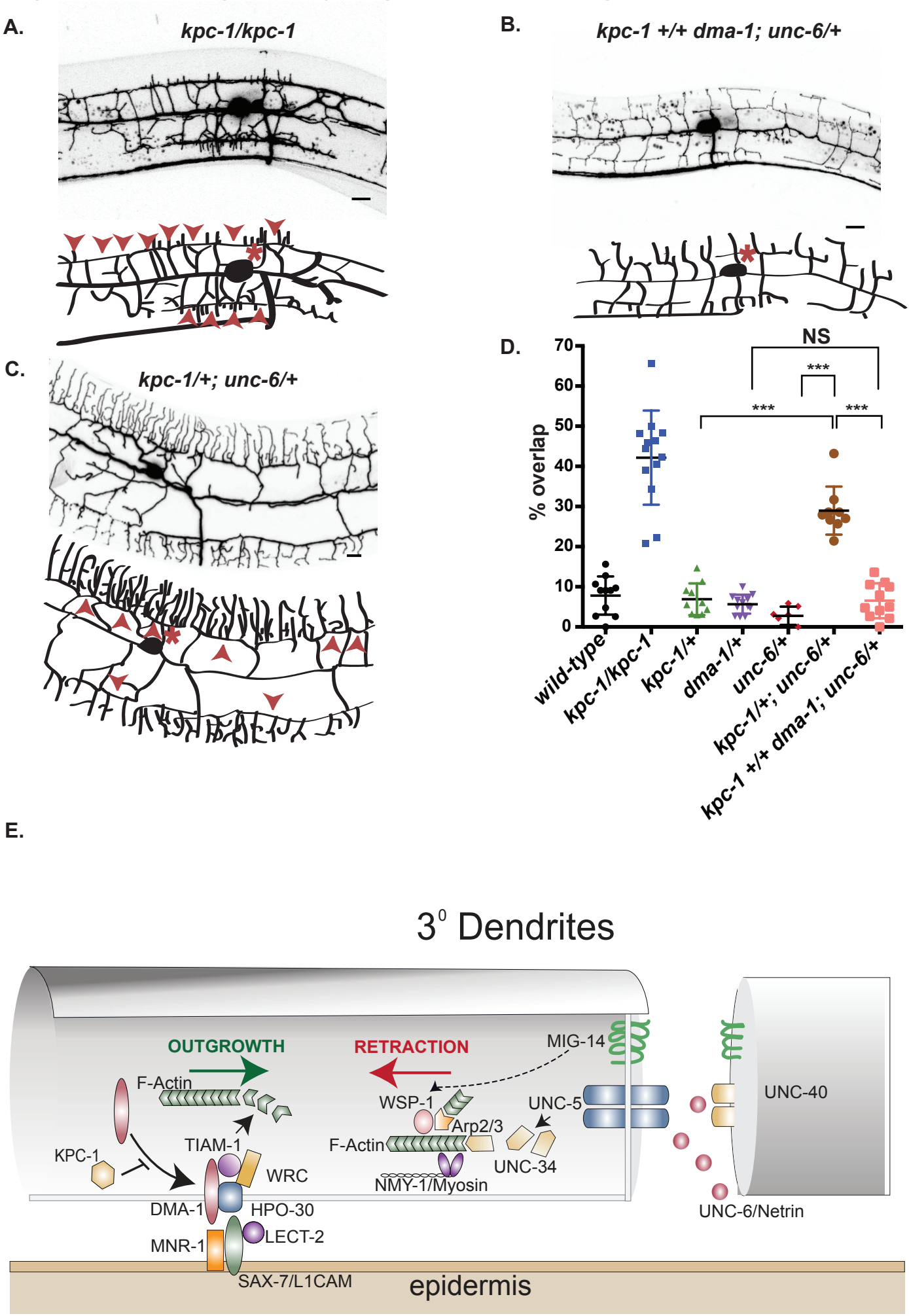
Figure 9: Opposing pathways regulate dendrite outgrowth and retraction.